The intensity of contrast enhanced Astra Gemini laser

Contact *joerg.schreiber@mpq.mpg.de*

J.H. Bin, W.J. Ma, C. Kreuzer, D. Kiefer, J. Meyer-ter-Vehn, and J. Schreiber
Department für Physik, Ludwig-Maximilians-Universität München, Garching, 85748, Germany
&
Max-Planck-Institut für Quantenoptik, Garching, 85748, Germany

M.J.V. Streeter, and Z. Najmudin
Blackett Laboratory, Imperial College London, SW7 2BZ, UK

M. Yeung, S. Cousens, B. Dromey, and M. Zepf
Queen's University of Belfast, Belfast, BT7 1NN, UK

P.S. Foster, C. Spindloe, and R. Pattathil
Central Laser Facility, Rutherford Appleton Laboratory, Chilton, Didcot, Oxon, 0X11 0QX, UK

Introduction

The intensity in the laser focus is one of the key issues in the high-intensity laser-solid interactions. Astra Gemini laser delivers more than 4 J in a single pulse with FWHM duration of 50 fs, allowing for laser intensities in excess of 5.6×10^{20}W/cm^2. Here we present a complete analysis on the measured laser focal spot image in a recent campaign employing nm-thin foils and calculate the actual laser intensity with experimental conditions. This analysis may explain why the ion energies obtained in this campaign were below 20 MeV, which at a first glance is puzzling by virtue of the large amount of laser energy delivered to the target. Compared to other laser systems, it also shows the need for adaptive optics to improve on this issue.

The rapid development of ultrahigh intense lasers opened a number of new interesting research field in laser-plasma interactions. One of the most important parameters is the actual laser intensity distribution, which will dramatically change the interaction process. For example, in laser driven ion acceleration, a change in the laser intensity will change the resulted ion energy significantly. And due to the experimental limitation, the laser intensity distribution is always imperfect and could be much lower in the perfect case. Thus detailed analysis to extract the actual laser intensity based on the measured laser focus image is essential in deducing the physical origin of the experimental observations. Here laser intensity distribution is analyzed in detail and several calculated laser intensity values are presented and discussed within the context of experimental observations.

Experimental set-up

The experiments have been performed with the ASTRA Gemini facility. This system delivers pulses with duration of 50 fs FWHM and central wavelength at 800 nm. A re-collimating double plasma mirror system was introduced to further enhance the laser contrast with a typical energy loss of 50 percent. An f/2 off-axis parabolic mirror (OAP) is used to focus the pulses to a measured full-width half maximum (FWHM) diameter spot size of 2.7×4.9 µm. Noted that the OAP has a 2 cm diameter hole in the centre for diagnostics of backscatted radiation. Due to losses in the beamline and the plasma mirrors, 4-5 joules of laser energy arrive on target. A Thomson parabola (TP) spectrometer was used at a distance of 0.3 m along the target normal direction in order to determine the ion spectrum. Diode array (DA) detectors were positioned at a distance of 30 cm behind the electric field plates to capture the ions. The DA has been absolutely calibrated at MLL Tandem accelerator. A Layer of 15 Al µm foil has been added in front of the DA to protect it from direct and scattered laser light.

Results and discussion

A typical laser focal spot image is shown in figure 1. In this beamtime, the laser focal spot was optimized to the tightest FWHM diameter spot size of 2.7×4.9 µm with an elliptical shape. The typical dynamic range for the laser focal imaging is about 2-3 orders of magnitude based on the ratio between the standard 16-bit camera used for focal imaging and the normal noise readout level of a few 100 counts. In order to enlarge the observed dynamic range, sequential unsaturated-saturated imaging was employed. As shown in figure 1 (b) and (c), a saturated focal image is obtained by irradiating the laser pulse through the imaging system with medium power (1 mJ) so as to saturate the centre part but keep the camera running without damage and get readout in the outer area; while the unsaturated image is sequentially obtained by attenuating the laser with a reflective optics, in our case, one special mirror with 5% reflectivity. The relative ratio could be also derived from data by comparing the readout values located in the same area of two images. The average ratio derived from the data is 21, which fits very well with the actual reflectivity of the mirror. Therefore, the dynamic range was further enhanced to be about 4 orders of magnitude by joining these two images. Based on this method, a peak intensity of 2.0×10^{20}W/cm^2 was obtained from the measured focal spot image with the laser pulse duration of 50 fs FWHM and 4.5 J laser energy on target.

The importance of the encircled laser energy ratio should be also stressed. The encircled energy ratio was calculated by comparing the integral quantities of the readout in the full image area detected by the camera and the readout inside the FWHM diameter. Therefore, the encircled energy ratio was calculated to be 0.18 from the focal spot image as seen from figure 2. We can calculate the mean laser intensity inside the FWHM diameter to be 1.2×10^{20}W/cm^2. Here the mean laser intensity is defined as $I_{mean} = \dfrac{E_{FWHM}}{d_1 \cdot d_2 \cdot \tau_{FWHM}}$, where E_{FWHM} is the encircled energy within FWHM spot, d_1 and d_2 are the FWHM diameter in both dimensions, τ_{FWHM} is the pulse duration.

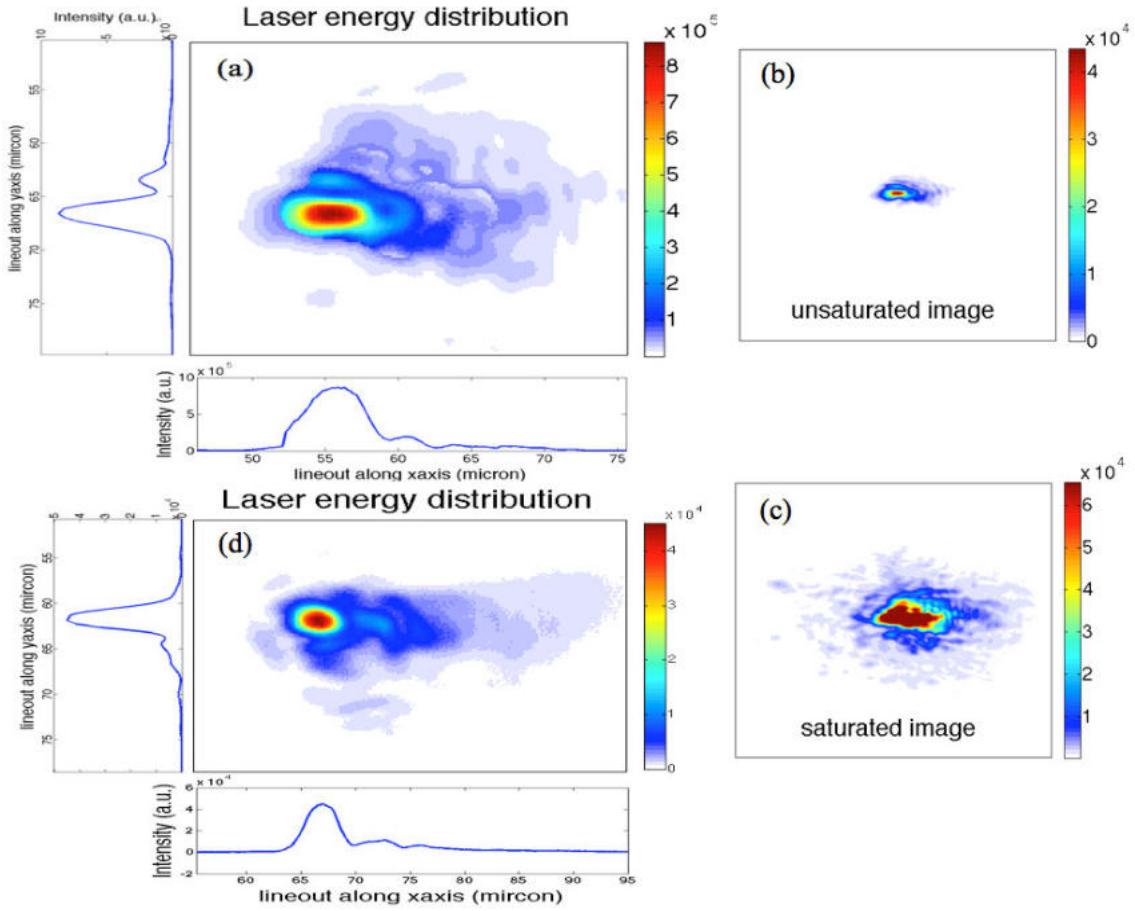

Figure 1: (a) Laser energy distribution with high dynamic range obtained with Astra Gemini laser by using sequential images of unsaturated focal spot image (b) and saturated focal spot image (c). (d) Laser energy distribution with a smaller focal spot by using a static corrector in latter experiment, without the adaptive optics system.

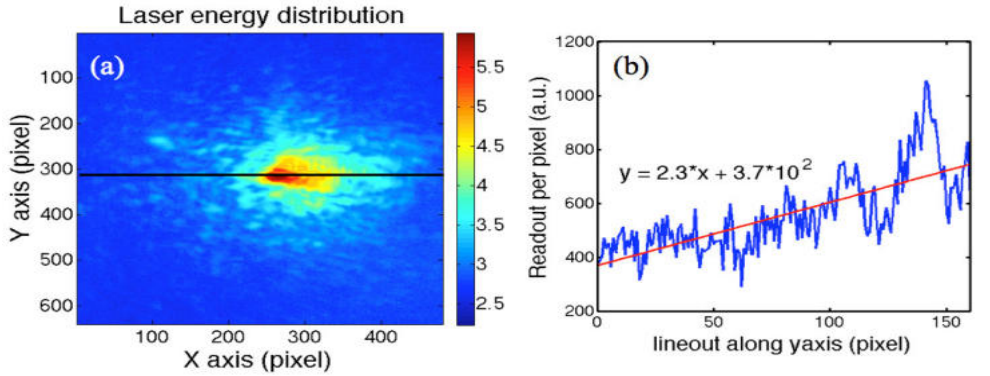

(c)	theoretic peak intensity for a perfect pulse	Measured peak intensity	encircled energy ratio	Mean intensity within FWHM diameter	Recalculated peak intensity	encircled energy ratio after consider the residual energy	Mean intensity after consider the residual energy
Astra Gemini	5.6×10^{20}w/cm^2	2.0×10^{20}w/cm^2	0.18	1.2×10^{20}w/cm^2	1.86×10^{20}w/cm^2	0.168	1.1×10^{20}w/cm^2

Figure 2: (a) Laser energy distribution in logarithmic scale. (b) Measured (blue) and fitted (red) curve for the readout per pixel. (c) Table for different relevant intensity values for Astra Gemini laser system. With the same conditions for a perfect Gaussian beam, the encircled energy ratio is 0.5.

Up to now, all the values related to the laser intensity distribution were calculated only considering the signals in the field of view of the camera. However, as can be seen from the logarithmic scaled laser energy distribution in figure 2 (a), the laser energy is distributed among the full field of view. A portion of the laser energy is distributed in an even wider field that is not recorded. We dub this portion the residual energy. A simple estimation of the residual energy can be done as follows. A linear curve is fitted to the readouts for each Y-axis value in the edge of the focal image, and then extrapolated to zero, which defines the residual energy area. By integration over this area, we obtain the residual energy value. One example is shown in figure 2 (b), the counts are taken along the black line shown in figure 2 (a). Thereby, the actual laser intensity values for the experiments were recalculated and listed in the table in comparison to the values without considering the residual energy as well as a theoretic peak intensity value for a perfect Gaussian pulse, as shown in figure 2 (c). While in latter experiments a static corrector was installed in the beamline to remove the aberrations. A smaller focal spot with FWHM diameter of 2.5×3.5 µm was achieved, yielding a peak intensity of 3.0×10^{20}W/cm^2, as shown in figure 1 (d). Noted that the adaptive optic (AO) system is not implemented for those experiments.

Summary

We have shown the complete analysis of the spatial laser energy distribution. The actual values are significantly reduced as compared to a laser with perfect Gaussian shape. To a certain extent, this residual energy may be attributed to the hole in the parabolic mirror. The obtained intensity explains some important experimental results. For example, the maximum proton energy obtained from nm-thin targets was not much greater than 10 MeV. This observation stresses the importance of the adaptive optic system that is developed for use in the Astra Gemini target area, which can significantly reduce the aberration in the laser beam and achieve the high intensity focal spot close to diffraction limit [1].

Acknowledgements

The authors would like to acknowledge the staff of the ASTRA Gemini operations team for the assistance during the experiment.

References

1. J.D. Alston et al., CLF annual report, in press (2012).

A two-screen spectrometer to measure the 3D momentum distribution of GeV electron beams produced by laser wakefield acceleration experiments on Astra Gemini

Contact *michael.bloom@imperial.ac.uk*

M. S. Bloom, M. J. V. Streeter, S. Kneip, A. Döpp, S. P. D. Mangles, Z. Najmudin, and H. Nakamura

The Blackett Laboratory, Imperial College London, London SW7 2AZ, UK

R. A. Bendoyro, J. Jiang and N. C. Lopes

GoLP/Instituto de Plasmas e Fusão Nuclear, Instituto Superior Técnico, Lisboa, Portugal

J. Holloway

High Energy Physics Group, University College London, London WC1E 6BT, UK

O. Cheklov, S. Hawkes, C. J. Hooker, V. A. Marshall, B. T. Parry, P. P. Rajeev and D. R. Symes, Y. Tang

Central Laser Facility, STFC, Rutherford Appleton Laboratory, Didcot OX11 0QX, UK

Introduction

Laser wake field accelerators (LWFAs) have great potential for future high-energy physics applications, as compact sources of high-energy particles, and as light sources[1 2 3]. This is in part due to their ability to sustain accelerating fields (> 100 GV / m) around three orders of magnitude greater than can be supported in conventional radio frequency accelerators (< 100 MV / m)[4].

LWFAs have potential as hard x-ray light sources, for applications such as phase contrast imaging as recent experiments have demonstrated[5 6]. As electrons are accelerated in a LWFA they can undergo transverse, or betatron, oscillations due to the strong focusing forces associated with non-linear wakefields[7], producing synchrotron radiation[8]. In the bubble regime[9] this is due to self-injected electrons retaining some transverse momentum on entering the bubble. This "betatron radiation" can be in the 10s of keV range with peak brightnesses comparable to 3rd generation synchrotron sources[3].

In previous experiments[10 11] it has been common to employ a collimator before the electron beam enters the bending magnet of the electron spectrometer. This is in order to stop electrons with positive or negative momentum in the magnets dispersion direction (i.e. electrons which exit the accelerator at an angle to the spectrometer axis). Such electrons can cause the beam energy to be over- or under-estimated (see figure 1). However in experiments producing and using betatron x-rays it is desirable to deflect the electrons away from the laser axis before they can impact on anything that would produce bremsstrahlung radiation. This makes the use of collimating apertures unsuitable for electron spectrometers for experiments were betatron radiation is important.

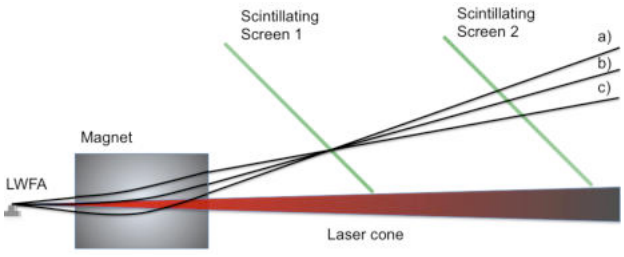

Figure 1: Three electron paths are shown which all impact screen 1 at the same position. b) Shows the path of an electron exiting the LWFA along the laser axis. a) Shows a higher energy electron exiting at a positive angle. c) Shows a lower energy electron exiting at a negative angle.

We have implemented a two-screen spectrometer method[12 13] to overcome this issue. The two-screen method allows the bending magnet to be placed close to the LWFA without a collimator. This allows the whole electron beam to pass between the magnet pole pieces without deteriorating the magnet performance, thereby reducing bremsstrahlung radiation. This geometry also produces sufficient deflection of electrons away from the laser axis reducing the chance of the electron beam colliding with x-ray detectors. This collimator-free two screen spectrometer still allows a reliable and full measurement of the electron energy to be produced. Furthermore the method allows all three momentum components of the electron beam to be measured which can provide insight into the acceleration and radiation generation mechanisms.

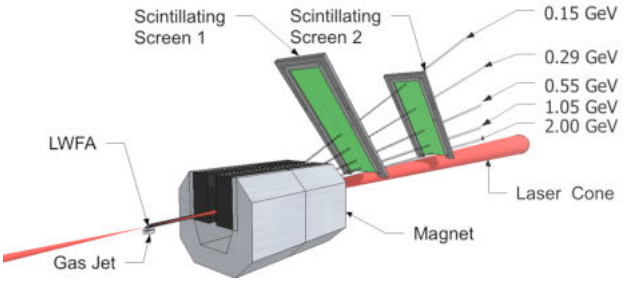

Figure 2: Experimental setup. Electrons of differing energies are shown passing through scintillating screens as calculated by tracking algorithm.

Two Screen Spectrometer

In this report we present a two screen spectrometer design for LWFA experiments on Astra Gemini. The magnet consists of rectangular pole pieces constructed from sintered neodymium blocks, mounted in a c-shaped yoke. This c-shape allows low energy electrons to leave the spectrometer without striking the yoke, further reducing the bremsstrahlung radiation produced. The pole piece separation is 25 mm. The magnet can be positioned so that the entire f/20 cone of the laser can pass through unimpeded, allowing optical diagnostic access to the transmitted laser pulse.

A map of the magnetic field was created using a hall probe and calibrated Teslameter. We find that the field maximum is 1.02 T in the mid-plane of the magnet with a field uniformity of 0.01 T r.m.s. over the central 200 mm of the magnet. The yoke design ensures that there is no field reversal along the electron propagation direction.

The magnet is constructed in two sections, each 150 mm long. In this experiment these were fixed together providing a single magnet 300 mm long. The magnet can be approximated by 1.02 T uniform rectangular magnet with an effective length of 288 mm. The magnet is mounted on motorized rails that allow

the magnet to be completely moved out of the electron beam path for measurements of for example, the electron beam profile.

As shown in Figure 1, electrons with different energies can strike the same point on a single screen due to differing exit angles. However with the inclusion of a second screen their energies and angles can be ascertained. Separating the exit angle from the electron energy is equivalent to measuring two components of the electron momentum, p_z, the electron momentum in the laser propagation direction and p_y, the electron momentum in the magnet dispersion direction. The third component of the electron momentum, p_x, can be recovered from the position of the electron beam on the screens in the direction perpendicular to the magnet dispersion direction.

Spectrometer Reconstruction Algorithm

The electron exit angle and energy can be calculated if it is known to pass through a given position on screen 1 and screen 2, s_1 and s_2 respectively. For many electrons incident of a screen identifying these positions is not trivial. One method of solving this problem is to place fiducials in the beam between the two screens, creating shadows in the images on the second screen. However this method has the disadvantage of not sampling the whole spectrum. Alternatively, as was done in this experiment, one can identify s_1 and s_2 points using clearly identifiable features in the electron spectrum. This works particularly well for electron spectra from self-injection experiments on Astra Gemini.

Once a feature has been identified and points s_1 and s_2 have been defined, the correct electron momentum and exit angle (or equivalently p_z and p_y are found by tracking electrons through the mapped magnetic field using the relativistic Lorentz force equation in an iterative process.

It can be shown that, for the magnetic field map of this spectrometer, electrons in the range of 1 MeV to 2 GeV will have a unique mapping of momentum vectors $[p_z, p_y]$ to positions on the screens $[s_1, s_2]$, as long as the electron source point is known (in this case the end of the gas jet). This would not necessarily be the case for highly non-uniform magnetic fields; in which case there is not a unique solution of the three momentum components for every value of s_1 and s_2.

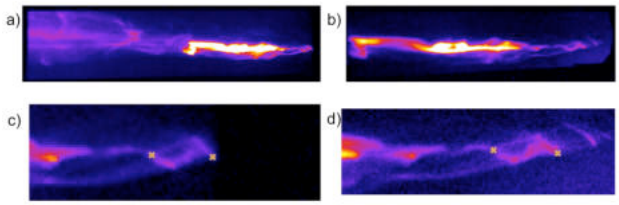

Figure 3: Images from a) screen 1 and b) screen 2 for a shot at $n_e = 5 \times 10^{19}$ cm^{-3} and a 10 mm gas jet nozzle, c) and d) show a smaller region. The marked point on the right corresponds to 1.34 ± 0.07 GeV electrons at an angle of -3 mrad. The marked point on the left corresponds to 1.09 ± 0.04 GeV at an angle of -1 mrad.

Experimental Results

The two screen magnetic spectrometer was fielded in an experiment using the Astra Gemini Laser in the Central Laser Facility at the Rutherford Appleton Laboratory. The 800nm (central wavelength) laser was focused using a f/20 off-axis parabolic mirror onto a super-sonic gas nozzle. This produced a 22 μm (**FWHM**) diameter focal spot with approximately 35% of the 12 J of laser energy contained inside the FWHM. The pulse duration of the laser was ≈55 fs. A 10 mm diameter gas nozzle was deployed to produce a region of helium which could be varied to produce an electron plasma density, when fully ionized, of up to $n_e = 8 \times 10^{18}$ cm^{-3}. The front of the magnet was placed 135 mm from the laser focus and two scintillating (Lanex regular) screens where placed ≈ 0.7 m and ≈1.3 m away from the interaction at 45° and imaged onto 12 bit CCD cameras (See figure 2). The cameras viewing the screens were triggered after the interaction but within the scintillator fluorescence lifetime[14] to avoid light coming directly from the interaction. Additional light shielding was used to avoid reflected laser light activating the scintillator.

High-energy electron beams were produced over a range of plasma densities. The electron beam typically produced significant features on the electron spectrometer screens due to betatron oscillations of the electron beam[15], example scintillator screen images are shown in figures 3 and 4.

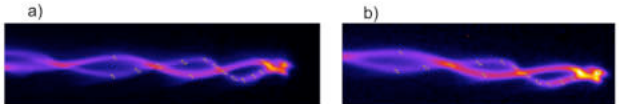

Figure 4: Images from a) screen 1 and b) screen 2 for a shot at $n_e = 2 \times 10^{18}$ cm^{-3} and a 15 mm gas jet nozzle. The marked points have their momentum components p_x, p_y and p_z plotted in figure 5.

Figure 3 shows the images from screens 1 and 2 for a shot at an electron plasma density of 5×10^{18} cm^{-3}, laser energy after amplification of 10.1 J, and a LWFA length of 10 mm, and results of the reconstruction method is shown. The error in this measurement was assessed: it was found that effects of positional error were greater than those from other sources such as the accuracy of the magnetic field measurement. By propagating the errors in the position for the screens, gas jet, plasma, magnet, and the human error in choosing clearly identifiable features in the spectra maximum bounds were found for s_1 and s_2; these maximum bounds were used in the reconstruction algorithm in order to find the limits shown in the reported error. Electrons were observed at energies as high as 1.34 ± 0.07 GeV on this shot. There are also features closer to the spectrometer axis that missed the first screen. The higher energy end of this spectrum shows clear betatron oscillations, responsible for the generation of bright x-rays.

Figure 4 shows images of the two scintillator screens for a shot at an electron plasma density of 2×10^{18} cm^{-3}, a laser energy of 11.3 J, but using a 15 mm diameter supersonic nozzle. This shot appears to show two interleaving beamlets. We have analysed the full 3D momentum distribution of a set of points for one of these beamlets. This is shown in figure 5.

The three dimensional momentum information about this beamlet shows that the oscillation is approximately confined to a plane and that this plane is almost 90º to the laser electric field direction, i.e. the strong betatron oscillations are not due to interaction with the laser field. There is a clear correlation between p_z and p_y, which can be interpreted as a "head-to-tail" tilt. Such tilts can be responsible for hosing instabilities in beam driven plasmas wakefield accelerators[16].

Preliminary simulations with Osiris do show that for extended plasma lengths the laser can be sufficiently depleted for the interaction to enter a "beam driven" phase (i.e. one where the electron beam itself drives a wakefield). However the resulting hosing does not show interleaving features in the electron beam. Such features are observed earlier in the interaction when the bubble undergoes rapid expansion due to modification of the laser strength by self-focusing, pulse compression and photon deceleration.

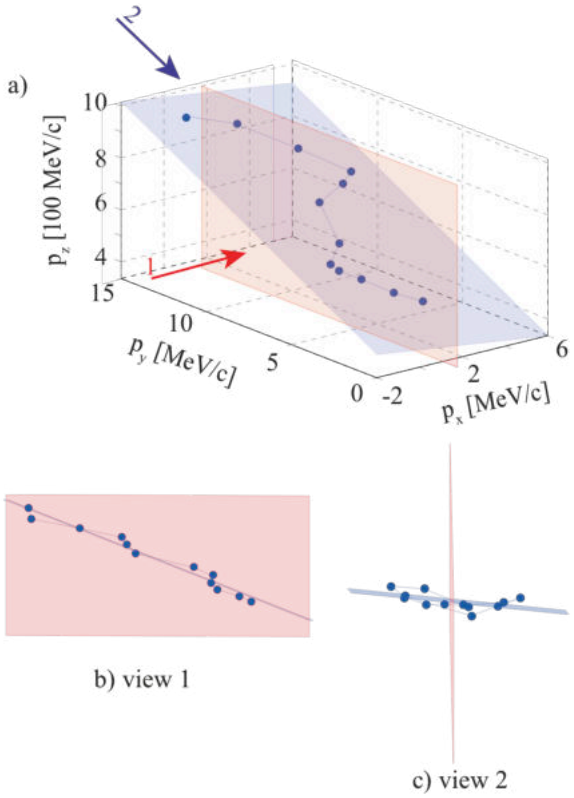

Figure 5: a) Three dimensional momentum distribution of one of the beamlets shown in figure 4. The blue points are 3D momentum coordinates of the identified features in the beam. The blue plane is the "plane of best-fit" to these points. The red plane corresponds to the laser electric field direction. Two additional views are shown (without axes) taken along the direction of the red and the blue arrows. b) shows the view along the red arrow (1), highlighting the "head-to-tail" tilt of the beam; c) shows the view along the blue arrow (2). This is a direction almost tangential to the red and blue planes, showing that the electrons are approximately distributed in a plane that is approximately at 90° to the laser electric field direction.

Conclusions

We have successfully fielded a two-screen spectrometer capable of measuring electron beams with energies greater than 1 GeV on Astra Gemini, having observed beams with features up to 1.34 ± 0.07 GeV. The two-screen method allows the full three dimensional momentum distribution of the beam to be examined which provides insight into the dynamics of electron injection and acceleration, vital for understanding the processes responsible for beam instabilities and x-ray generation.

Acknowledgements

The authors would like to thank the staff of the CLF for their excellent work without which this work could not have been carried out.

References

[1] W.P. Leemans, B. Nagler, A.J. Gonsalves, *et al.*, Nature Physics **2**, 696-699 (2006).
[2] E. Esarey, C.B. Schroeder, and W.P. Leemans, Reviews of Modern Physics **81**, 1229-1285 (2009).
[3] S. Kneip, C. McGuffey, J.L. Martins, *et al.*, Nature Physics **6**, 980-983 (2010).
[4] T. Tajima and J.M. Dawson, Physical Review Letters **43**, (1979).
[5] S. Corde, K. Phuoc, R. Fitour, *et al.*, Physical Review Letters **107**, (2011).
[6] S. Kneip, C. McGuffey, F. Dollar, *et al.*, Applied Physics Letters **99**, 093701 (2011).
[7] I. Kostyukov, A. Pukhov, and S. Kiselev, Physics of Plasmas **11**, 5256-5264 (2004).
[8] A.G.R. Thomas, Physics of Plasmas **17**, 056708 (2010).
[9] A. Pukhov and J. Meyer-ter-Vehn, Applied Physics B-Lasers and Optics **74**, 355-361 (2002).
[10] S.P.D. Mangles, C.D. Murphy, Z. Najmudin, *et al.*, Nature **431**, 535-538 (2004).
[11] S. Kneip, S.R. Nagel, C. Bellei, *et al.*, Physical Review Letters **103**, 35002 (2009).
[12] I. Blumenfeld, C.E. Clayton, F.J. Decker, *et al.*, Nature **445**, 741-744 (2007).
[13] D.H. Froula, C.E. Clayton, T. Doppner, *et al.*, Physical Review Letters **103**, 215006 (2009).
[14] A.G. Glendinning, S.G. Hunt, and D.E. Bonnett, Physics in Medicine and Biology **46**, 517-530 (2001).
[15] S.P.D. Mangles, G. Genoud, S. Kneip, *et al.*, Applied Physics Letters **95**, 181106 (2009).
[16] C. Huang, W. Lu, M. Zhou, *et al.*, Physical Review Letters **99**, 1-4 (2007).

Near-GeV electron energy acceleration in low density plasma channels

Contact *simon.hooker@physics.ox.ac.uk*

PA Walker, N Bourgeois, W Rittershofer, J Cowley, SM Hooker
Dept. of Physics, Clarendon Laboratory, University of Oxford, Oxford, OX1 3PU, UK

N Kajumba, AR Maier, J Wenz, CM Werle, S Karsch, F Grüner
Dept. für Physik, Ludwig-Maximilians-Universität München, Geschwister-Scholl-Platz 1, 80539 Munich, Germany

DR Symes, PP Rajeev, SJ Hawkes, O Chekhlov, CJ Hooker, B Parry, Y Tang, VA Marshall, RJ Clarke
Central Laser Facility, STFC Rutherford Appleton Laboratory, Didcot OX11 0QX, UK

Introduction

The acceleration gradients achieved in laser-driven plasma accelerators are three or more orders of magnitudes greater than provided by conventional accelerators, offering a route to a new class of compact accelerators. To date electron beams have been generated with energies up to the GeV level in accelerators a few cm long [1-3]. Having reached this milestone, attention is turning to increasing the energy gain per stage and improving the shot-to-shot reproducibility of the electron beams in order that they may be used to drive applications.

In laser-driven plasma accelerators, the difference in the phase velocity of the plasma wave and the velocity of the electrons causes the accelerated electron bunch to move from an accelerating phase to decelerating one after the dephasing length $L_d = \frac{4}{3}(\omega_0^2/\omega_p^3)\sqrt{a_0}$, where ω_0 and ω_p are the angular laser and plasma frequencies respectively, and a_0 is the normalized vector potential of the laser field. Since the peak accelerating electric field is proportional to ω_p the maximum energy gain per stage is proportional to $1/\omega_p^2 \propto 1/n_e$, where n_e is the plasma density. For these reasons there is considerable interest in driving plasma accelerators at lower plasma densities and over longer distances. In the experiments described here a hydrogen-filled capillary discharge waveguide [4,5] was used to form a plasma channel, extending the distance over which the plasma wave could be driven.

In this report we describe experiments with the Astra-Gemini laser on acceleration driven with plasma channels formed in a capillary discharge waveguide. These show improved reproducibility and also injection and acceleration of electrons at the lowest plasma densities reported to date, a result which is promising for future experiments with greater energy gain per stage.

Experimental Set-up

The experiment was performed with the North beam of the Astra-Gemini laser, as shown schematically in Figure 1. Laser pulses were focused by an f = 3m off-axis paraboloid, used at f/20, to the entrance plane of the capillary waveguide. The transmitted laser light was reflected onto the optical diagnostic table via a wedge, into which was drilled a hole which allowed accelerated electrons to pass to an electron spectrometer. The optical diagnostic table incorporated: (i) a CCD camera to image the laser spot; (ii) a photodiode to measure the transmitted laser energy; (iii) an optical spectrometer; and (iv) a Grenouille to measure the laser pulse length after the plasma interaction.

In these experiments the capillaries were laser-machined in sapphire blocks, and were 33mm long and of 300 μm diameter. The hydrogen gas was ionized, and the plasma channel formed, by applying a discharge pulse with a peak current of 500A and 200 ns half-period

For these experiments the laser beam was apodized to improve the focal spot quality; this was successful in that the fraction of energy contained within the half-peak-intensity contour of the focal spot was measured to be 38% compared to 50% expected for an ideal Gaussian beam. However, the apodization limited the maximum on-target energy to 4.2 J, of which (0.38/0.5) × 4.2J =3.2 J can be considered to be contained within low-order modes. The FWHM duration of the laser pulse was measured to be τ = 55 fs, corresponding to a maximum incident peak power of P = 60 TW and a peak intensity at focus of I = 3.3 x 10^{18} Wcm^{-2}.

The energy spectrum of electrons accelerated within the plasma channel was measured with a two-magnet spectrometer as described elsewhere this issue. Immediately in front of the spectrometer was positioned a thin Lanex screen, which allowed the position and angle of electrons entering the magnet to be measured. This information was used to correct the electron energy for variations in the electron beam pointing. Electrons dispersed by the magnetic spectrometer were detected by CCD cameras recording the phosphorescence from the Lanex screens.

Results

Figure 2 shows the maximum recorded electron energy as a function of the axial plasma density n_e, which can be found from the initial gas pressure from interferometrically-measured scaling laws for the waveguide [6]. Acceleration is observed in three regimes: (i) at high plasma densities the laser power $> P_c^{diff}$, where P_c^{diff} is the critical power for *self-guiding* [2], and hence the plasma channel plays little role in guiding the laser pulses; (ii) a hybrid regime for which $P_c < P < P_c^{diff}$, where P_c is the critical power for relativistic *self-focusing*; (iii) a low-density regime in which $P < P_c$ and hence only the plasma channel can guide the laser pulse.

It is noticeable that the electron beam energy exhibits an optimum plasma density, at which electrons with energies up to 900 MeV are observed. This optimum plasma density may be understood as follows. For high electron densities the length of the plasma channel L_c is longer than the dephasing length, and hence electrons are accelerated up to the dephasing length, and then decelerated until the end of the channel is reached. In this regime, decreasing the plasma density will increase the output electron energy, as is observed, until the plasma density corresponds to $L_c \approx L_d$. The density yielding the maximum electron energy is very close to this condition; if anything the highest electron energies are obtained for slightly larger plasma densities, which makes sense if electron injection occurs a short distance after the start of the plasma channel. For electron densities below the optimal value, $L_c < L_d$, the electron energy is expected to be given approximately by $W = W_{max}(\frac{L_c}{L_d}) \propto 1/n_e$, where W_{max} is the energy gain achieved in one dephasing length. Figure 2 shows this theoretical dependency in blue as well as a fit to data points on the low pressure side of the peak (black) which is in good agreement with the expected inverse dependence of electron energy on plasma density.

It is noteworthy that electron beams were generated for plasma densities as low as 3.25 x 10^{17} cm^{-3}. To our knowledge this is the lowest density at which electron injection and acceleration has been observed, and suggests that if the length of the plasma channel were properly matched to the dephasing length electrons with energies significantly above 1 GeV would have been generated.

The reproducibility of the generated electron beams was studied by recording the electron energy spectra for 36 consecutive shots with the same timing and initial gas pressure. The laser arrived at the capillary at the peak of the discharge current with the plasma density set to 2.15 x 10^{18} cm^{-3}. Figure 3 shows raw images of the electron spectrometer Lanex screens for these shots, illustrating that high-energy electron beams were generated on every laser shot. These electron spectra are uncorrected for variations in the laser energy (typically between 5 and 10%), laser pointing (pointing jitter typically 60% of laser spot size, i.e. 24μm) or electron beam pointing (typically 3 mrad). Figure 4 shows the variation of the maximum electron beam energy as a function of laser pulse energy for these 36 consecutive shots, showing that, as expected, the electron beam energy increases with the laser pulse energy. Hence at least some of the fluctuations observed in the energy spectra of Fig. 3 are due to variations in the laser beam energy; variations in the pointing of the input laser pulse and the output electron beams are also likely to be responsible for much of the observed shot-to-shot variations in the measured energy spectrum.

Finally we note that the divergences of the electron beams were measured to be approximately 3.5 mrad (FWHM) which is lower than divergences obtained in most gas jet experiments.

Conclusions

In conclusion, the Astra-Gemini laser was used to study electron acceleration in plasma channels formed in a capillary discharge waveguide. Electrons with energies up to 900 MeV were generated, and the variation of the maximum electron beam energy with the plasma density was found to agree with a simple model of acceleration and deceleration in a plasma channel. The generated electron beams exhibited good reproducibility.

Acknowledgements

The authors would like to thank MS Bloom, MJV Streeter, S Kneip, Z Najmudin and SPD Mangles from Imperial College London for their assistance in setting up and calibrating shared diagnostics, as well as P Brummit, A Zayyani, D Rathbone, D Neville and D Rose from the Rutherford Appleton Laboratory engineering department for help in setting up.

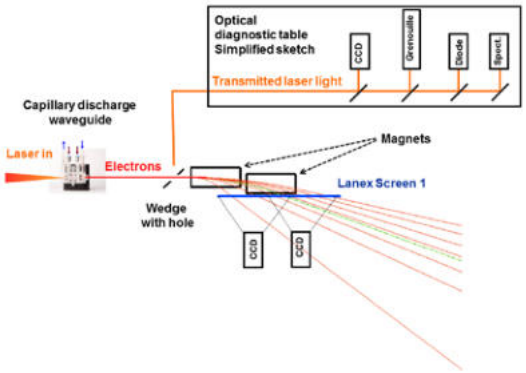

Figure 1. The sketch of the experimental set-up at the Astra Gemini target area.

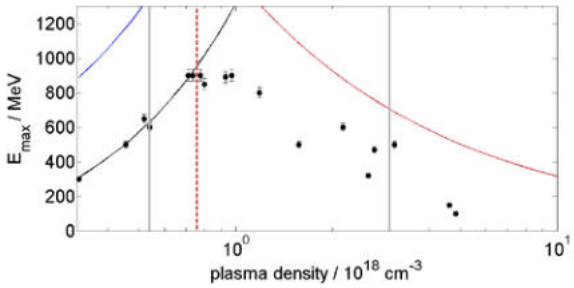

Figure 2. The maximum recorded electron energy as a function of the axial plasma density. The density for which the dephasing length equals the capillary length is shown by the dotted red line. The three different regimes discussed in the text are separated by solid grey lines. The solid red line shows the expected electron energy after acceleration over one dephasing length, assuming that the laser pulse self-focuses to the matched spot size in the bubble regime [2, 7]. For the low-density regime the black solid line is a fit to the data showing good agreement with the expected inverse linear dependence of electron energy on plasma density. The electron energy expected due to $L_c < L_d$ is shown in blue.

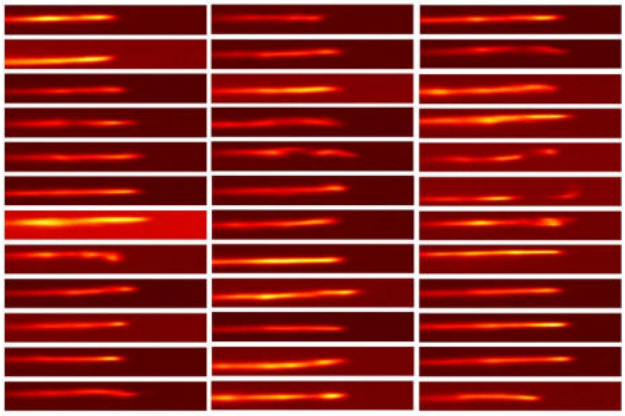

Figure 3. Electron spectra from 36 consecutive shots are shown. For each image the horizontal axis is increasing energy from left to right.

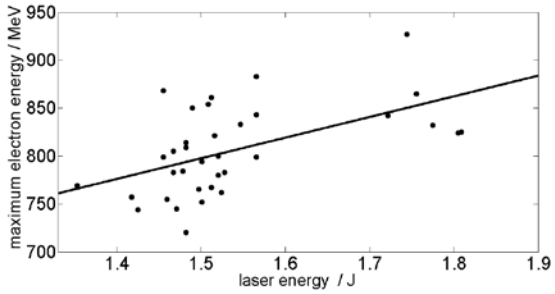

Figure 4. The maximum electron energy vs the laser energy within the FWHM of the laser spot.

References

1. W.P. Leemans *et al., Nat Phys* **2**, 696 (2006)
2. T.B.A Ibbotson *et al., Phys.Rev.ST Accel. Beams* **13** (2010)
3. S. Kneip *et al., Phys. Rev. Lett.* **103**, 035002 (2009)
4. D.J. Spence and S.M. Hooker, *Phys. Rev. E* **63**, 015401(R) (2000)
5. A. Butler, D.J. Spence and S.M. Hooker, *Phys. Rev. Lett.* **89**, 185003 (2002)
6. A.J. Gonsalves *et al., Phys. Rev. Lett.* **98**, 025002 (2007)
7. W. Lu *et al., Phys.Rev.ST Accel. Beams* **10**, 061301 (2007)

A two-screen electron spectrometer for broad- and narrow-bandwidth electron spectra

Contact *simon.hooker@physics.ox.ac.uk*

PA Walker, N Bourgeois, W Rittershofer, J Cowley, SM Hooker

Dept. of Physics, Clarendon Laboratory, University of Oxford, Oxford, OX1 3PU, UK

N Kajumba, AR Maier, J Wenz, CM Werle, S Karsch, F Grüner

Dept. für Physik, Ludwig-Maximilians-Universität München, Geschwister-Scholl-Platz 1, 80539 Munich, Germany

DR Symes, PP Rajeev, SJ Hawkes, O Chekhlov, CJ Hooker, B Parry, Y Tang, VA Marshall, RJ Clarke

Central Laser Facility, STFC Rutherford Appleton Laboratory, Didcot OX11 0QX, UK

Introduction

Magnetic dipole spectrometers are widely used to measure the energy spectrum of electron beams generated in laser plasma accelerators. In essence they comprise: (i) a region of known magnetic field in which electrons are deflected according to the Lorentz force and (ii) an imaging screen on which the deflected electrons are detected. In laser wakefield acceleration experiments, the screens most often used are image plates (IPs) and Lanex scintillating screens.

Imaging plates have the advantage of being absolutely calibrated for charge and high spatial resolution (< 10um). However, they are relatively expensive and the read-out time is long: after every exposure the IP has to be transported to an IP reader, read-out and blanked. Depending on the spatial resolution required, and size of the IP, this process can take between a few minutes to an hour. Further IPs have to be protected against room light since this erases the signal on the imaging plate.

Lanex scintillating screens have the advantage of being cheap and readily available. With these screens, CCD cameras are used to image the phosphorescence excited by the incident electron beam. Lanex screens are therefore convenient since the signal they generate can be recorded in situ. However, calibrating the Lanex signal against charge requires either: accurate calibration of the light collecting efficiency and detection sensitivity of the imaging system and camera [1]; or cross-calibration against an image plate [2].

In order to calculate the electron energy from a measurement of its deflection by the magnetic field, the position and propagation vector of the electron as it enters the magnetic field must be known. In the absence of this information it must be assumed that the incident electrons propagate along the laser axis. However, in practice the electrons emerging from a laser-driven accelerator can propagate at an angle to the laser axis, leading to errors in the deduced energy. There is therefore interest in devising techniques for non-destructive measurement of the electron beam propagation on every laser shot. In this report we describe two methods by which this can be done.

Experimental Set-up and Method

In this work the North beam of the Astra-Gemini laser was used to generate electrons, with energies up to 900 MeV, in the plasma channels formed by a capillary discharge waveguide [3, 4]. A more detailed account of this experiment is described in another report by the authors in this CLF Annual Report.

The magnetic field of the spectrometer was provided by two permanent dipole magnets. The magnetic field of either of the magnets was 1 T strong with dimensions of 0.4 m by 0.15 m by 0.04 m. The deflected electron beams were detected by Lanex screens, the phosphorescence from which was imaged by a pair of CCD cameras.

Figure 1 illustrates the two methods used to provide simultaneous electron beam energy and pointing information. Figure 1(a) shows a thin Lanex screen (the "Pointing Lanex") positioned before the entrance to the electron spectrometer, the fluorescence from which is imaged by a CCD camera. If it is assumed that the electron beam originates from the centre of the exit of the plasma waveguide, which is known to much less than the capillary diameter (300 μm), measurement of the position of the electron beam at the spectrometer entrance gives the position and propagation vector of the beam as it enters the spectrometer. From this information – and field maps of the dipole magnets – the energy calibration of the spectrometer can be calculated for each shot.

Figure 1(b) shows an alternative arrangement in which the electron bunch position at the entrance of the spectrometer is deduced from imaging the electrons on two screens located *after* the dipole magnets. This method also yields all the information needed to deduce the entry point and propagation vector of the electron bunch as it enters the magnetic field [5], although different procedures are required for monoenergetic and broad-band electron spectra. For a monoenergetic beam, reconstruction of the incident beam path proceeds as follows. The beam illuminates one point on each of the two screens, and since the beam trajectory in this field-free region is a straight line, the point and propagation vector of the beam as it leaves the magnetic field may be deduced. From this information the trajectory through the magnetic field may be calculated for a given electron energy, and hence the apparent position and propagation vector of the electron beam in the exit plane of the capillary can be found. The retrieval algorithm then adjusts the energy of the electron beam until the position of the electron beam in the exit plane of the capillary is closest to the centre of the capillary; this yields the energy of the beam and the energy calibration of the spectrometer for that shot.

This approach cannot be used with broad-band electron beams since the energy spectra have no distinguishing features. To overcome this lead bars were placed between the two Lanex screens in order to imprint holes into the energy spectrum recorded by the second Lanex screen. The known locations of the lead bars and the measured positions of the spectral holes could then be used to calibrate the spectrometer using the same algorithm as used for monoenergetic electron beams. Note that the (corrected) energy spectrum recorded by Lanex Screen 1 is unaffected by the lead bars.

Results

Figure 2(a) shows an example of the energy correction determined by the Pointing Lanex method. The uncorrected beam spectrum has a peak at 692 MeV, but correction for the off-axis pointing of the electron beam increases this to 757 MeV, i.e. an increase of 9%. We note that this method was very easy to implement and, at least for these relatively high electron beam energies, scattering of the electron beam by the Pointing Lanex did not appreciably degrade the recorded energy spectrum.

Figure 2(b) illustrates correction using 2-screens method; in this case correction leads to an increase in the energy of the peak by

8% to 247 MeV. It is worth noting that for this method it was found that the beam charges had to be above 20 pC in order for the spectrum recorded by Lanex Screen 2 to be measurable. Further, if the electron beam propagated at large angles to the system axis it missed the second Lanex screen, preventing correction of the energy spectrum recorded on Lanex Screen 1. We also note that the two-screen method requires significant additional space – in our case approximately 1 m – behind the dipole magnets.

Conclusions

In conclusion two methods for correcting for the effects on the measured energy spectrum of off-axis electron beam propagation were investigated. Both methods were demonstrated successfully, and for the conditions of this experiment both yielded energy corrections of about 10%. Of the two methods, the use of a Pointing Lanex was found to be particularly convenient, and was found not to degrade the recorded energy spectrum.

Material Used

The scintillating screens used were Lanex Intensifying Screen Regular manufactured by Kodak. The CCD cameras were 12 bit Flea2 CCD cameras with a chip size of 1624 X 1224 pixels each 4.4 µm by 4.4 µm large manufactured by Point Grey. The bandpass interference filters had a center wavelength of 550 nm with a bandwidth of 50 nm and were manufactured by Edmund Optics. The imaging plates used to determine the charge of the electron bunches were Fuji Imaging Plates of type BAS-MS.

Acknowledgements

The authors want to thank Darren Neville and Dave Rose for assistance in setting-up the magnets.

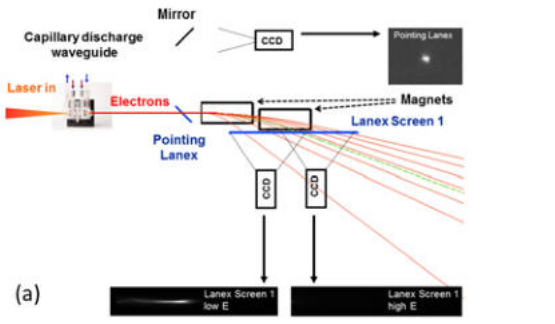

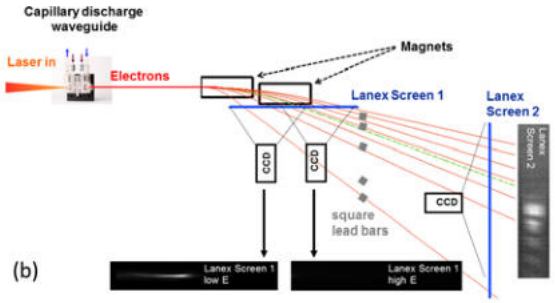

Figure 1. Sketch of the experimental set-up for the Pointing Lanex (a) and the two-screen (b) methods of energy correction.

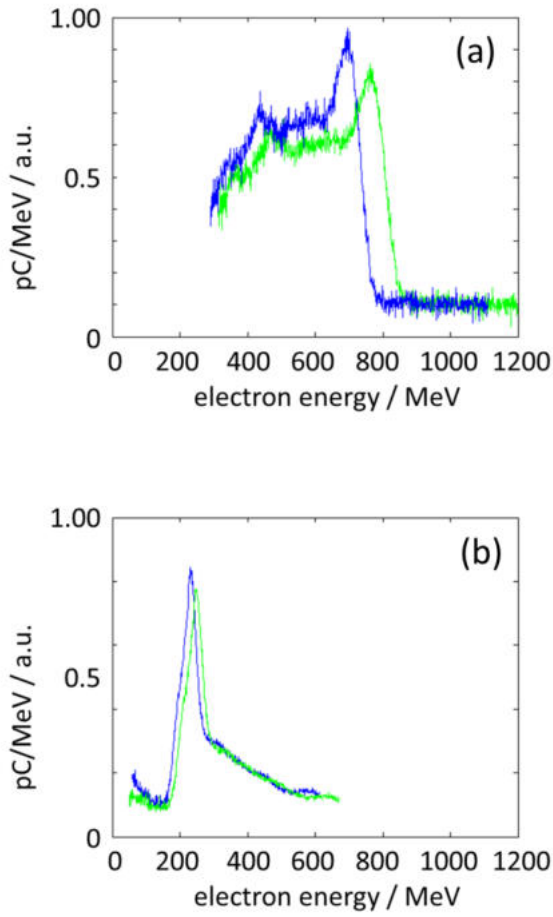

Figure 2. Examples of electron energy spectra recorded before (blue) and after (green) correction for off-axis propagation of the electron beam propagation by the Pointing Lanex (a) and two-screen (b) methods.

References

1. A. Buck *et al., Rev. Sci. Instrum.* **81**, 033301 (2010)
2. K. Zeil *et al., Rev. Sci. Instrum.* **81**, 013307 (2010)
3. D.J. Spence and S.M. Hooker, *Phys. Rev. E* **63**, 015401(R) (2000)
4. A. Butler, D.J. Spence and S.M. Hooker, *Phys. Rev. Lett.* **89**, 185003 (2002)
5. C. E. Clayton *et al., Phys. Rev. Lett.* **105**, 105003 (2010)

Electron acceleration up to 2 GeV in plasma channels

Contact nelson.lopes@ist.utl.pt

N. C. Lopes, C. Russo, R. A. Bendoyro, J. Jiang, N. Lemos, J. M. Dias, J. Vieira, L. O. Silva

GoLP / IPFN / Instituto Superior Técnico
Av. Rovisco Pais, Lisboa, Portugal

M. S. Bloom, J. Cole, S. Kneip, S.P.D. Mangles, Z. Najmudin
The Blackett Laboratory, Imperial College
London, SW7 2 BZ, UK

D. R. Symes, P. Foster, R. Pattathil, S. Hawkes, C. Hooker, B. Parry, O. Checkhlov, Y. Tang

Central Laser Facility, STFC, Rutherford Appleton Laboratory
Didcot, Oxon OX11 0QX, UK

Introduction

Laser wakefield accelerators (LWFA) were proposed in 1979 by Tajima and Dawson [1] and have received renewed interest since the demonstration of mono-energetic electron bunches in 2004 [2-4] and with the demonstration of GeV energy gains [5,6]. These electron beams have been used in applications from electron radiography [7] to the generation of XUV radiation in periodic magnetic structures [8] and X or Gamma rays generated by the betatron oscillations of the electron beams in the ion channel left in the laser wake [9-10].

In a LWFA, the goal is to create a relativistically moving plasma structure with GV/cm electric fields capable to accelerate trapped electrons to high energies. To maximize the efficiency of the acceleration process and provide stable acceleration structures, the laser pulse duration and spot size must match the wavelength of the electron plasma waves. Additionally, a minimum normalized vector potential a_0 of about 2 is required. At these moderate laser intensities, an external guiding mechanism to keep the laser pulse focused in the plasma over a length close to the maximum acceleration length is required. The guiding mechanism consists of the pre-formation of a plasma channel with a radial parabolic density profile that acts on the laser in the same way as an index-graded fiber-optic, effectively cancelling the diffraction. Different techniques to create plasma channels adequate for LWFA have been proposed and tested from laser-based [11,12] to discharge-based plasma channels [13-15]. Discharge-based plasma channels present significant practical advantages over laser-based ones, as the former do not require additional independent laser beams and can be developed and operated independently of a complex laser system.

By increasing a_0 from 2 to about 4 while keeping the relation between plasma density and laser-pulse dimensions, the laser beam can be self-guided and the necessity of a plasma channel is removed. Moreover, wave-breaking and injection of charge into the relativistic plasma structure becomes possible, which results in the production of high energy electron bunches.

These two regimes, external guiding (EG) and self-guiding/self-injection (SGSI) can complement each other in a double-stage accelerator. SGSI is able to generate relativistic electron bunches and is therefore adequate for the first stage. EG transfers the laser energy into accelerated particle more efficiently but requires external injection and laser guiding [16], being therefore most adequate for a (purely accelerating) second stage. However, coupling both stages is a challenging task, raising concern over the practical details on injecting both the electron and laser beams in the second stage with the necessary pointing precision and synchronization.

In this paper we report the results of an experiment performed at the Astra-Gemini facility, which tested the use of gas cells for both SGSI and EG, thus testing two of the main pieces of a double stage accelerator. Structured gas cells of 2 cm and 4 cm lengths have been tested. It was found that it was possible to produce reproducible low energy spread electron bunches with energies of 500 MeV and a few pC charge in a SGSI configuration and on the other hand energy gains of up to 2 GeV were obtained in a configuration close to EG.

Experimental setup

The results reported in this paper were obtained using one beam of the Astra-Gemini laser system as a driver for the plasma wakefield. The laser pulse duration was 45-50 fs. Originally with a diameter of 150 mm, the beam was apodized by a soft aperture before the compressor to a diameter of 72 mm, leading to energies in the range 4.2-5.0 J. The beam was focused to a spot size estimated to be in the range W_0= 35 - 40 μm ($1/e^2$) corresponding to a maximum intensity in the range 2.5 - 3.2 x10^{18} W/cm^2. The target consisted of a gas cell similar to the cell described in [15]. A scheme of the gas cell can be seen in figure 1.

The gas cell consists of a rectangular box made of dielectric material, featuring an optical axis collinear with the laser beam. In the direction of the optical axis, the cell is limited by two conical electrodes and with 300 μm diameter drillings. For the results reported in this paper we have used gas cells with an electrode gap of 4 cm. The cells contain a sequence of dielectric thin plates spaced by 2.5 mm. The plates contain drillings with a diameter of 300 μm that are aligned with the optical axis and that are used to define the position and diameter of the initial plasma. The time required for filling the cell with gas (< 5 ms) is shorter that the time required the gas takes to leak through the electrode apertures (>50 ms), which allows for operation under pulsed gas injection.

The gas cells are equipped with optical-grade windows that allow transverse optical probing (e.g. interferometry). The electrodes of the gas cell are connected to the high-power transmission line for the main discharge. Optionally, the electrodes can also be connected to slow HV pulses, which are used to create a partially ionized plasma cloud on the optical axis a few milliseconds before the main discharge and that have been found to improve the uniformity and reproducibility of the plasma [17]. Since the HV pulse generator behaves as a short-circuit for pulses longer than 200 ns, the slow discharge is isolated from the HV pulse generator by a spark-gap.

The HV pulse generator is similar to that described in [15], except for the fact that the capacitor bank has 35 nF, the transmission line transformer has a set of 16 transmission lines with a length of 10 meters and with an impedance of 50 Ohm grouped in 4 groups of 4. Overall, the pulse generator leads to a multiplication of the capacitor voltage by 4 and has an output

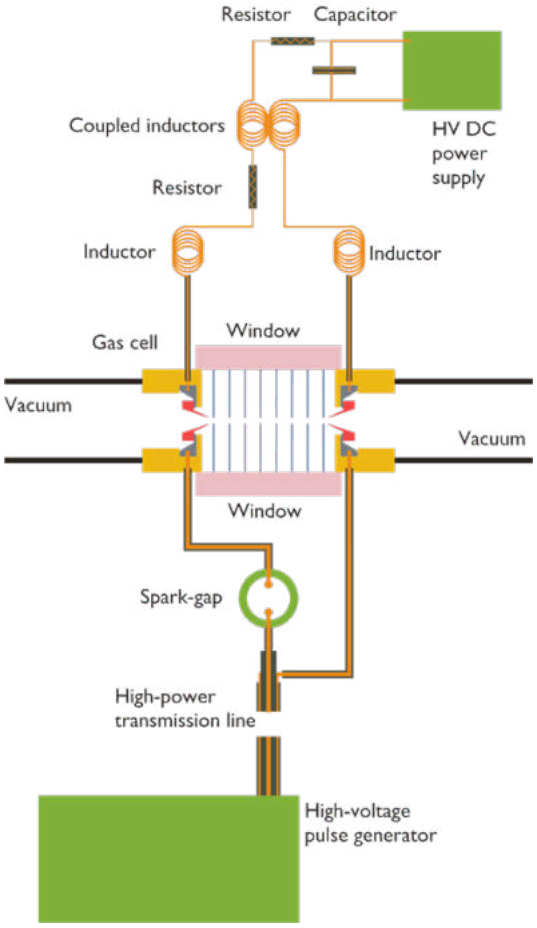

Figure 1. Scheme of the gas cell used in the experiment including the electric circuits for the pre-formation of the plasma channel.

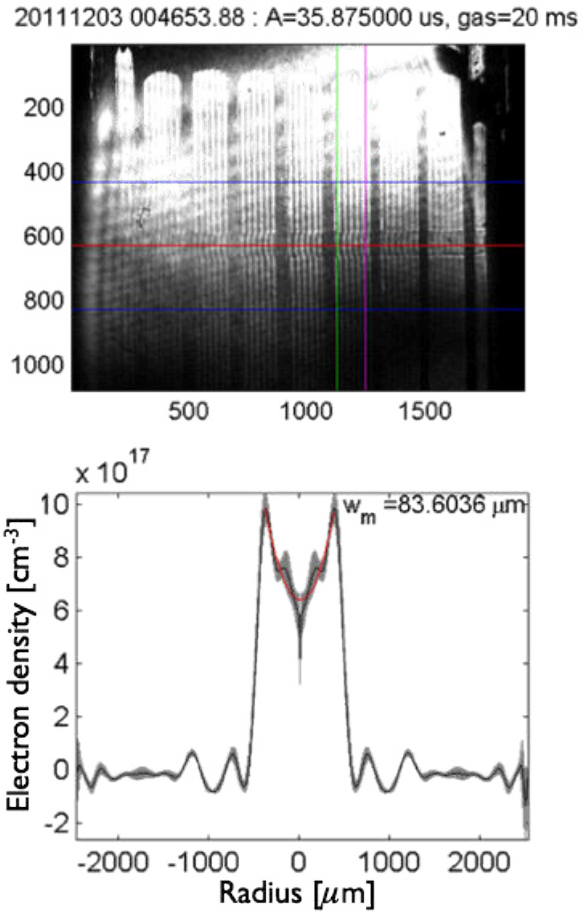

Figure 2. Pre-formed plasma channel. Picture of the interferometry diagnostic including the region selected to measure the plasma density and lineout of the plasma density profile obtained by Abel inversion of the interferogram phase.

impedance of 50 Ohm. In these experiments the charging voltage was limited to 25 kV, resulting in pulses with durations of 200 ns and maximum voltages and currents of 100 kV and 2 kA.

The more relevant diagnostics used in this experiment were the discharge current sensors (current transformers), the plasma density diagnostic (mack-zender interferometer using a fraction of the main beam), and the electron energy diagnostic (electron spectrometer with two gaps with 1 T and a length of 20 cm and two lanex screens)[18].

Electron acceleration in plasma channels

Plasma channels have been produced by HV discharges on gas cells filled with hydrogen for different values of pressure, voltage and delay between discharge and laser pulse. As an example, in Figure 2 we present a plasma channel obtained with parameters optimized for the external guided regime. In this case, an initial pressure of 100 mbar corresponding to a density of 2.4×10^{18} H_2 molecules per cm^3 was used. A lineout of the plasma channel density radial profile, obtained after a 100 ns delay between plasma breakdown and laser probing, is also presented in Figure 2. This channel has an electron density on axis of 6.5×10^{17} cm^{-3} and a low-power matched propagation spot size of 84 mm.

As expected, there was no trapping of electrons for low-density plasma channels. However, increasing the pressure of the gas cell resulted in the production of electron beams with very broad spectra. In Figure 3 we present six shots where electron beams have been produced. The initial pressure and laser energy were respectively: 1) 200 mbar, 4.93 J; 2) 160 mbar, 4.90 J; 3) 212 mbar, 4.66 J; 4) 275 mbar, 4.65 J; 5) 275 mbar, 4.66 J; 6) 262 mbar, 4.40 J. Although the number of shots is low, we have some evidence that the maximum electron energy is obtained for the shots with initial pressure close to 200 mbar. The maximum electron energy measured was 2 GeV, with an error estimated in +150 MeV and -400 MeV. This error bar for energy (for shots 1 and 3) is the maximum error obtained by considering a maximum beam angle of 5 mrad with the propagation direction, consistent beam pointing measurements obtained in a screen without magnetic field (see next section). Moreover, with absence of clear features in the spectra it was not possible to use both screens to retrieve the electron beam angle and measure the energy with more accuracy. For lower and higher initial pressures, we have measured maximum energies in the range 1-1.5 GeV (shots 2 and 4-6 in Figure 3). The electron charge, for the selected six shots, was estimated to be close to 20 pC .

It was not possible to measure the plasma density profiles of the plasma channels for these shots. However we can estimate that axial plasma electron density was close to 8×10^{17} cm^{-3} for shots 1 and 2. Also the low intensity matched propagation spot size should be significantly smaller than 84 mm found for 100 mbar [17].

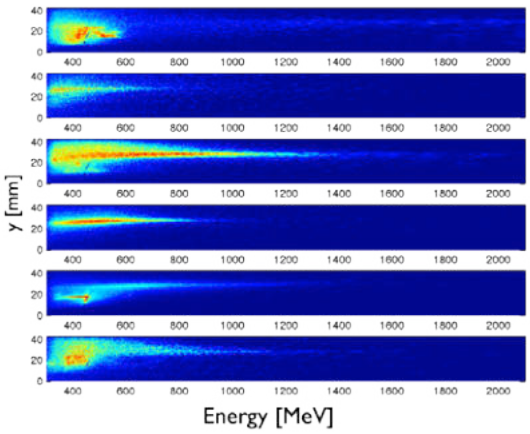

Figure 3. Energy spectra of electrons produced by LWFA in a plasma channel with maximum energies up to 2 GeV in shots 1 and 3.

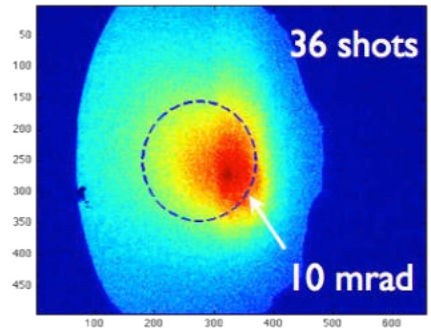

Figure 4. Signal accumulated during 36 shots in a lanex screen distant 1.5 m from the interaction point (electron spectrometer magnets removed), a circle with 10 mrad deviation angle was added to the picture.

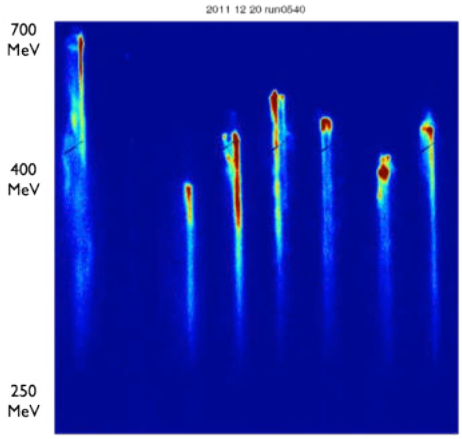

Figure 5. Eight images of a selected region of the second electron spectrometer screen for shot with parameters in the table 1.

Table 1: Parameters of eight selected shots with electron energy spectra showing monoenergetic features

Shot	Laser energy [J]	H_2 density first sub cell [10^{18} cm^{-3}]	H_2 density remaining cells [10^{18} cm^{-3}]	Max electron energy [MeV]
1	4.37	5.4	3.6	660
2	4.35	5.4	0	605
3	4.52	5.4	2.1	410
4	4.49	5.4	1.5	470
5	4.80	5.4	1.5	545
6	4.55	5.4	1.5	500
7	4.33	5.7	1.5	430
8	4.34	6.0	1.5	485

Electron beams in long gas cells

In order to test the possibility of using these cells as a first stage of a LWFA, the same gas cell was used without a preformed gas channel (HV switched off) at higher plasma density (gas cell pressure).

First, by using a lanex screen at a distance of 1.5 m from the target (and with the electron spectometer magnets removed) we have established that the electron beams produced for a wide range of parameters were in a circle corresponding to an angular radius of 10 mrad. The divergence of each individual beam strongly depends on the cell pressure and varied between 2 mrad and about 20 mrad.

In Figure 5, we present 8 shots selected from a single run in which we tried to optimize the energy dispersion. We injected a higher density of H2 in the first sub-cell (about 5.5 x 10^{18} cm^{-3}) and lower density in the remaining sub-cells. In this experiment, it was not possible to retrieve the electron density by interferometry, however a negative gradient in the density is likely to happen with such parameters, especially in the first sub-cells (the lengths of the sub cells are 0.2 mm for the first and 2.5 mm for the remaining). The shot energy and H_2 densities for the shots of Figure 5 are presented in Table 1. The last 5 shots were made at same pressure and they have an average maximum energy of 486 MeV and a variability of 10% (for a variability of the laser energy of 4.5%). However, if we exclude the shots with higher and lower energies (shots 5 and 7) and using only shots 4, 6 and 8 the max energy variability becomes 3.3 % (for a variability of the laser energy of 2.7%).

The charge on the shots of figure 5 is estimated to be in the range 0.5-2.5 pC [19]. The energy spread of the last shot is 1.5% by neglecting the low charge tail.

Conclusions

In conclusion we have demonstrated two of the basic building locks of a double stage LWFA: a first self-injection stage producing few percent energy spread electron bunches with energies close to 500 MeV and a second externally guided stage with energy gains up to 2 GeV.

The characterization of each acceleration stage is incomplete and each stage can be further optimized in order to improve not only the parameters of the produced beams but also to make a double stage LWFA possible. With that in mind, the more important parameters to optimize are the beam pointing stability of both laser and electron beams as well as the charge of the electron bunches produced in the first stage.

Acknowledgements

The research leading to these results has received funding from LASERLAB-EUROPE (grant agreement no. 284464, EC's Seventh Framework Programme). This work was also partially supported by Fundação para a Ciência e Tecnologia (Portugal).

References

1. T. Tajima and J. M. Dawson, Laser Electron Accelerator, Phys. Rev. Lett. **43**, 267-270 (1979)
2. Mangles S. P. D. *et al*., Monoenergetic beams of relativistic electrons from intense laser-plasma interactions, Nature **431**, 535-538 (2004)
3. Geddes, C. G. R. *et al*., High-quality electron beams from a laser wakefield accelerator using plasma-channel guiding, Nature **431**, 538-541 (2004)
4. Faure, J. *et al*., A laser-plasma accelerator producing monoenergetic electron beams, Nature **431**, 541-544 (2004)
5. Leemans, W. P. *et al*., GeV electron beams from a centimetre-scale, Nat. Phys. **2**, 696-699 (2006)
6. Kneip, S. *et al*., Near-GeV Acceleration of Electrons by a Nonlinear Plasma Wave Driven by a Self-Guided Laser Pulse, Phys. Rev. Lett. **103**, 035002 (2009)
7. Mangles, S. P. D. *et al*., Table-top laser-plasma acceleration as an electron radiography source, Laser and Particle Beams **24**, 185-190 (2006)
8. Fuchs, M. *et al*., Laser-driven soft-X-ray undulator source, Nat. Phys. **5**, 826-829 (2009)
9. Kneip, S. *et al*., Bright spatially coherent synchrotron X-rays from a table-top source, Nat. Phys. **6**, 980-983 (2010)
10. Cipiccia, S. *et al*., Gamma-rays from harmonically resonant betatron oscillations in a plasma wake, Nat. Phys. **7**, 867-871 (2011)
11. Durfee, C. G. and Milchberg, H. M., Light pipe for high intensity laser pulses, Phys. Rev. Lett. **71**, 2409-24012 (1993)
12. Volfbeyn, P. *et al*., Guiding of laser pulses in plasma channels created by the ignitor-heater technique, Physics of Plasmas **6**, 2269-2277 (1999)
13. Spence, D. J. and Hooker, S. M., Investigation of a hydrogen plasma waveguide, Phys. Rev. E **63**, 015401 (2000)
14. Bendoyro, R.A. *et al*., Plasma channels produced by a laser-triggered high-voltage discharge, Phys. Rev. E **68**, 035402 (2003)
15. Bendoyro, R.A *et al*., Plasma Channels for Electron Accelerators Using Discharges in Structured Gas Cells, Plasma Science, IEEE Transactions on **36**, 1728-1733 (2008)
16. Lu, W. *et al*., Generating multi-GeV electron bunches using single stage laser wakefield acceleration in a 3D nonlinear regime, Phys. Rev. ST Accel. Beams **10**, 061301 (2007)
17. C. Russo. *et al*., to be published (2012)
18. Bloom, M. S. *et al*., A two screen spectrometer to measure the full 3D momentum distribution of GeV electron beams produced by laser Wakefield acceleration experiments on Astra Gemini, CLF annual report 2011-2012.
19. Glinec, Y. *et al*., Absolute calibration for a broad range single shot electron spectrometer, Rev. Sci. Intr. **77**, 103301 (2006)

Calibration of grazing-incidence flat-field soft x-ray diffraction gratings

Contact *imazono.takashi@jaea.go.jp*

T. Imazono, A. S. Pirozhkov, M. Kando, A. Ya. Faenov, T. A. Pikuz, T. Kawachi, K. Ogura, Y. Hayashi, H. Kotaki, M. Koike, H. Daido, Y. Kato, S. V. Bulanov

Quantum Beam Science Directorate, Japan Atomic Energy Agency
8-1-7 Umemidai, Kizugawa, Kyoto 619-0215, Japan

P. Gallegos, J. Green, P. Foster, C. Brenner, D. R. Symes, P. Rajeev, D. Neely

Central Laser Facility, STFC Rutherford Appleton Laboratory
Chilton, Didcot, Oxon OX11 0QX, UK

E. N. Ragozin

P. N. Lebedev Physical Institute of the Russian Academy of Sciences
53 Leninsky Prospekt, Moscow 119991, Russia

Introduction

Grating-based x-ray and soft x-ray spectrographs are widely used for photometric measurements and plasma diagnostics in various laser-plasma experiments, including research on plasma and ion spectroscopy [1-3], x-ray lasers [4-7], high-order harmonics generation in various regimes [8-11], and so on. In most cases, it is necessary to know throughput of the spectrograph to make quantitative data analysis. Among the factors contributing to throughput diffraction efficiency of the grating is typically the least known factor and the efficiency is subject to change with time.

In recent study, we performed the experiments on a novel regime of high-order harmonics generation by high-power (10-200 TW) relativistic-irradiance (>10^{18} W/cm^2) laser pulses in gas jet targets [11] using the Astra Gemini laser [12] in the CLF, RAL, UK and the J-KAREN laser [13] in Kansai Photon Science Institute (KPSI), JAEA, Japan. In these experiments, three blazed-type varied-line-spacing (VLS) replica gratings installed in flat-field soft x-ray spectrographs were used. All gratings have been used for long terms. Also it has passed long periods since the diffraction efficiency of the gratings were initially evaluated [14-17]. It is important to measure the efficiency of gratings used in an experiment each time because there is the possibility that the optical properties are degraded.

Here we report the measurements of diffraction efficiency of three gratings, which are two 1200 lines/mm gratings and a 2400 lines/mm grating, using a reflectometer installed at the soft x-ray beamline (BL-11) [18] of SR Center of Ritsumeikan University, Shiga, Japan. The measurements were performed in the spectral ranges from 1.8 nm to 24 nm for the first, second, and third spectral orders of the gratings. It is supposed to be a rather low efficiency compared to those of the measurements performed in the earlier experiments [14-17]. We also provide the data of the sagittal uniformity of the efficiency across one of the gratings.

Evaluation beamline for soft x-ray optical components

The BL-11 beamline has been operated to measure the wavelength and angular characteristics of the absolute reflectivity (or diffraction efficiency) of soft x-ray optical components such as thin films, multilayer mirrors, gratings, polarizing elements, etc. It consists of four systems: prefocus, monochromator, reflectometer, and control [18]. Its overall length from the source point to the reflectometer is about 10 m.

The prefocus system comprises beam-defining apertures and Kirkpatrick-Baez focusing mirrors. The light beam is focused on the entrance slit, S1, horizontally by the spherical mirror M1 and vertically by the spherical mirror, M2.

One of the outstanding features of the monochromator system is a wide wavelength range between 0.5 nm and 25 nm achieved by incorporating two types of Monk-Gillieson (M-G) monochromators. One is a conventional M-G monochromator equipped with three laminar-type VLS holographic plane gratings [19] G1 (300 lines/mm), G2 (600 lines/mm), and G3 (1200 lines/mm). These gratings are used interchangeably at the included angle of either 176° or 172°, depending on the required scanning range. One particular included angle is easily selected by inserting the vertical focusing spherical mirror, M3 or M5, into the beam at an angle of incidence of 88° or 86°. The various combinations of these gratings and mirrors make it possible to cover the wavelength range of 1.2-25 nm. The second monochromator is a new type with a constant-line-spacing holographic plane grating, G4 (600 lines/mm), used at an included angle of 176° that employs a scanning mechanism based on surface normal rotation and it can cover the wavelength range of 0.5-2 nm [20].

The monochromatized beam emerging from the exit slit, S2, is focused onto a sample placed in the reflectometer by the toroidal mirror M6. A filter-chamber is located between S2 and M6 in order to reduce the unwanted higher harmonics and stray lights. Thin films of Fe, Ti, C, B, Si, Al, Cr, and Ni (nominal thickness of 0.5-μm) are currently set in it.

The reflectometer system consists of a modified θ-2θ reflectometer/diffractometer. The sample stage (XYZθ-stage) can control the incident angle and position. The reflected (or diffracted) beam from the sample is detected by a silicon photodiode (AXUV-100G, IRD Inc.) having an effective area of 10 × 10 mm^2 mounted on the 2θ-arm, where the detection area can be specified by vertical and horizontal apertures in front of the detector. All axis of X, Y, Z, θ, and 2θ can be controlled independently. Also the control of the monochromator and reflectometer can be performed synchronously by the control system.

Grazing-incidence soft x-ray flat-field gratings

We calibrated two 1200 lines/mm gratings and a 2400 lines/mm grating, which were the blazed-type mechanically ruled replica gratings fabricated by Hitachi, Ltd. All the gratings are coated with Au. The 1200 lines/mm gratings have the same part number. The detailed specifications are listed in Table 1. These gratings have been employed in the experiments on high-order harmonics generation by high-power relativistic-irradiance laser pulses in gas jet targets [11]. One of the gratings with the 1200 lines/mm groove density has been used at CLF, RAL

Table 1: Specifications of two kinds of VLS replica gratings. The notations of N, R, θ_B, λ_B, α, and R_λ mean effective groove density (mm^{-1}), radius of curvature (mm), blaze angle (°), blaze wavelength (nm), mounting standard incidence angle (°), and wavelength range with flat-field focusing (nm), respectively.

Part No.	N	R	θ_B	λ_B	α	R_λ
001-0266	1,200	5,649	10.0	3.2	87.00	5-20
001-0471	2,400	15,920	1.5	1.9	88.65	1-5

(hereinafter refer to as $G12_{CLF}$) [14, 15]. The others, i.e., the 1200 lines/mm and 2400 lines/mm gratings have been used at KPSI, JAEA, hereinafter called as $G12_{KPSI}$ and $G24_{KPSI}$, respectively [11]. The $G12_{KPSI}$, $G24_{KPSI}$, and $G12_{CLF}$ were calibrated at the incidence angles used in the experiments [11], i.e., of 87.0°, 88.65°, and 84.6°, respectively.

Diffraction efficiency measurements

The measurement of diffraction efficiency in a wavelength range between 1.8 nm and 24 nm was carried out using the conventional M-G monochromator with the G1 grating and M5 mirror. The beam-defining apertures of BL-11 were set to 6 mm (H) × 3 mm (V), which corresponded to the acceptance angles of 3 mrad (H) × 2 mrad (V), respectively. The degree of linear polarization at around 14 nm has been quantitatively determined to be about 90% by polarization analysis [21]. Thin films of Fe, Ti, C, B, Si, and Al were used as filters in the wavelength ranges of 1.8-3.3 nm, 2.8-5.2 nm, 4-8 nm, 6-14 nm, 12-20 nm, and 17-24 nm, respectively. The spectral resolution was a couple of hundred. The incident beam on the sample in the reflectometer was focused to approximately 0.5 × 0.5 mm^2, as evaluated by the visible white light from the monochromator. The vertical and horizontal apertures in front of the detector were fully opened.

Two types of measurements were performed. Firstly, the angles of incidence of $G12_{KPSI}$, $G24_{KPSI}$, and $G12_{CLF}$ were fixed at θ = 87.0°, 88.65°, and 84.6°. The diffraction angles, 2θ, were changed along with the wavelength following the grating equation (spectral properties of the first, second, and third diffraction order lights).

Figure 1 shows the measured diffraction efficiencies for the spectral orders m = 1, 2, and 3 of $G12_{KPSI}$ at θ = 87.0° indicated by solid lines. For the reference, the diffraction efficiencies for m = 1 and 2 of a blazed replica grating measured at the same incidence angle are also shown by dashed lines, [16] although we note that the grating had the same part number but was not the same as $G12_{KPSI}$. The diffraction efficiencies for m = 1 and 2 are rather low but the spectral profiles show very similar behaviour to those of the earlier results, such as comparable efficiency for both orders in the 6-8 nm range. The higher efficiency for m = 2 than that for m = 1 around 5 nm is also represented well. The efficiency of m = 3 order is smaller, but its use contributes to high resolution of the spectrograph.

Figure 2 shows the measured diffraction efficiencies for the spectral orders m = 1, 2, and 3 of $G24_{KPSI}$ at θ = 88.65°. For the reference, the diffraction efficiencies for m = 1, 2, and 3 of a blazed replica grating, which had the same part number but was not the same as $G24_{KPSI}$, measured at the same incidence angle in the earlier experiment [17] are also shown by dashed lines. All efficiencies are lower than measured previously, but the slope is very similar to the earlier results. The noise stands out in the efficiency curves for m = 2 and 3 at around 4 nm. It is caused by the decreased intensity of the incident beam due to carbon-contamination on the surfaces of the mirrors and grating installed in the beamline.

Figure 3 shows the diffraction efficiencies of $G12_{CLF}$. Solid lines indicate those for the spectral orders m = 1, 2, and 3 at θ = 84.6° measured at BL-11. The dots are the efficiencies for m = 1, 2, and 3 at θ = 86.0° obtained by the earlier measurements at the Daresbury synchrotron facility [14]. Unfortunately the diffraction efficiency at θ = 84.6° has not been measured in the earlier experiments. The respective curves at θ = 84.6° and 86.0° are similar but the absolute values are different. The result shows that it is difficult to estimate the absolute diffraction efficiency at θ = 84.6° based on the data at another angle. In addition, it is important to re-evaluate the grating used in the experiment in the case that there is a possibility of degradation of optical properties due to long-term use [14].

Measurement of diffraction efficiency uniformity

Secondly, the uniformity of diffraction efficiency of the $G12_{CLF}$ grating was evaluated using BL-11 because it has two narrow strips caused by laser irradiation. Figure 4 shows the position dependence of diffraction efficiencies for m = 1 and 2 sagittally across $G12_{CLF}$ at θ = 84.6°. The wavelength was fixed at λ =

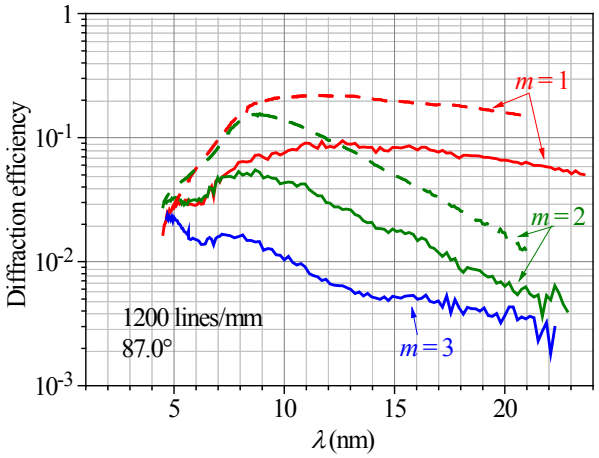

Fig. 1 Solid lines: measured diffraction efficiencies for the spectral orders m = 1, 2, and 3 of $G12_{KPSI}$ at θ = 87.0°. Dashed line: reference data for m = 1 and 2 from the earlier measurement [16].

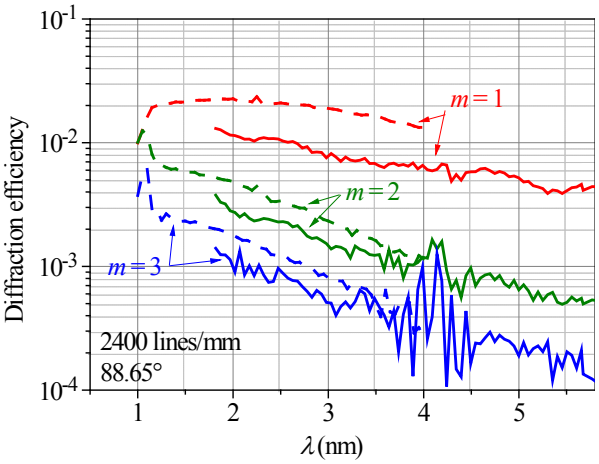

Fig. 2 Solid lines: measured diffraction efficiencies for the spectral orders m = 1, 2, and 3 of $G24_{KPSI}$ at θ = 88.65°. Dashed line: reference data for m = 1, 2, and 3 from the earlier experiment [17].

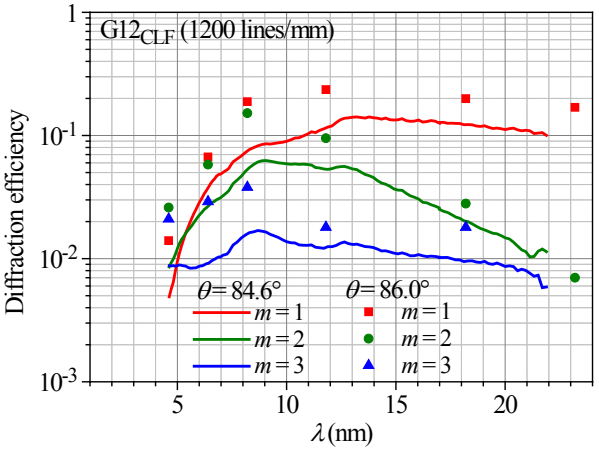

Fig. 3 Lines: diffraction efficiencies for the spectral orders m = 1, 2, and 3 of $G12_{CLF}$ at θ = 84.6° measured at BL-11. Dots: earlier measurements at θ = 86.0° [14].

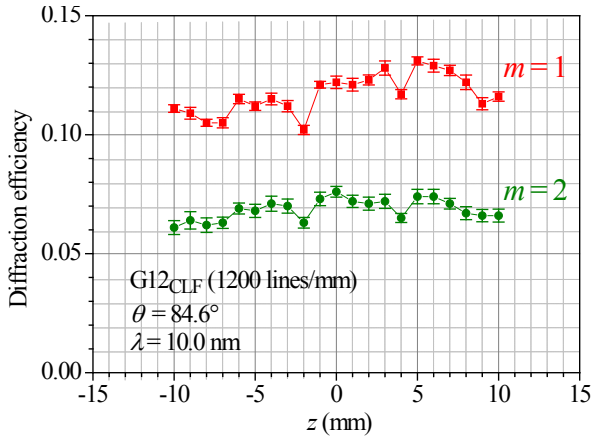

Fig.4 Position dependence of diffraction efficiencies for the spectral orders m = 1 and 2 measured parallel to the groove directions of $G12_{CLF}$, at fixed λ = 10.0 nm, θ = 84.6°, 2θ = 164.2° for m =1 and 2θ = 160.9° for m =2.

10.0 nm. The measurements was performed at the diffraction angle 2θ = 164.2° and 160.9° for m = 1 and 2, respectively. The position of z = 0 mm corresponds to the grating centre. We found that the efficiency uniformity sagittally across the grating is relatively good, although there are shallow dips observed at z = −2 and 4 mm corresponding to the visible strips.

Conclusions

In conclusion, we measured diffraction efficiencies of three flat-field blazed gratings employed in a number of high-power laser experiments. We matched the measurement conditions, such as the wavelength range, incidence angle, and diffraction orders, with the conditions in the experiments on high-order harmonics generation performed at CLF, RAL and KPSI, JAEA. We noticed rather lower diffraction efficiencies than those in the earlier measurements [14-17]. Also the efficiency uniformity of the grating used at CLF is found to be good, despite the strips visible on the grating surface. The reported results are indispensable for accurate measurements of x-ray spectra and quantitative data analysis. We conclude that the diffraction efficiencies of gratings used in experiments should be evaluated as frequently as possible.

Acknowledgements

We acknowledge the financial support from MEXT (Kakenhi 20244065, 21604008, 21740302, and 23740413), JAEA President Grant, and STFC (facility access funding).

References

1. H. A. Rowland, "On a Table of Standard Wave Lengths of the Spectral Lines," *Memoirs of the American Academy of Arts and Sciences* **12**, 101-186 (1896).
2. R. L. Kelly, "Atomic Emission Lines Below 2000 Angstroms. Hydrogen Through Argon," Report No. NRL--6648, (1968).
3. E. N. Ragozin, *et al.*, "Stigmatic high-resolution high-throughput narrow-band diffraction spectrograph employing X-ray multilayer mirrors," *Phys. Scripta* **47**, 495 (1993).
4. D. L. Matthews, *et al.*, "Demonstration of a Soft X-Ray Amplifier," *Phys. Rev. Lett.* **54**, 110 (1985).
5. S. Suckewer, *et al.*, "Amplification of stimulated soft x-ray emission in a confined plasma column," *Phys. Rev. Lett.* **55**, 1753 (1985).
6. R. Kodama, *et al.*, "Generation of Small-Divergence Soft X-Ray Laser by Plasma Waveguiding with a Curved Target," *Phys. Rev. Lett.* **73**, 3215 (1994).
7. H Daido, "Review of soft x-ray laser researches and developments," *Rep. Prog. Phys.* **65**, 1513 (2002).
8. A. McPherson, *et al.*, "Studies of multiphoton production of vacuum-ultraviolet radiation in the rare gases," *J. Opt. Soc. Am. B* **4**, 595(1987).
9. S. G. Preston, *et al.*, "Generation of bright, extreme-ultraviolet harmonic radiation from a krypton fluoride laser," *J. Phys. B* **31**, 1069 (1998).
10. B. Dromey, *et al.*, "Diffraction-limited performance and focusing of high harmonics from relativistic plasmas," *Nature Phys.* **5**, 146 (2009).
11. A. S. Pirozhkov *et al.*, "Soft-X-Ray Harmonic Comb from Relativistic Electron Spikes," *Phys. Rev. Lett.* **108**, 135004 (2012).
12. C. J. Hooker *et al.*, "The Astra Gemini project -- A dual-beam petawatt Ti:Sapphire laser system," *J. Phys. IV France* **133**, 673 (2006).
13. H. Kiriyama *et al.* "High-contrast, high-intensity laser pulse generation using a nonlinear preamplifier in a Ti : sapphire laser system," *Opt. Lett.* **33**, 645 (2008).
14. D. Neely, D. Chambers, F. Quinn and M. Roper, "Soft X-ray grating calibration," *RAL Technical Report* April (1997).
15. D. Neely *et al.*, "A multi-channel soft X-ray flat-field spectrometer," *AIP Conf. Proc.* **426**, 479 (1998).
16. T. Yamazaki *et al.*, "Comparison of mechanically ruled versus holographically varied line-spacing gratings for a soft-x-ray flat-field spectrograph," *Appl. Opt.* **38**, 4001 (1999).
17. M. Koike et al., "Performance of laminar-type holographic grating for a soft x-ray flat-field spectrograph in the 0.7–6 nm region," *Appl. Opt.* **74**, 1156 (2003).
18. M. Koike *et al.*, "New evaluation beamline for soft x-ray optical elements," *Rev. Sci. Instrum.* **73**, 1541 (2002).
19. M. Koike *et al.*, "Plane gratings for high-resolution grazing-incidence monochromators: holographic grating versus mechanically ruled varied-line-spacing grating," *Appl. Opt.* **36**, 6308 (1997).
20. M. Koike *et al.*, "Grazing-Incidence Monk-Gillieson Monochromator Based on Surface Normal Rotation of a Varied-Line-Spacing Grating," *Appl. Opt.* **41** 245 (2002).
21. T. Imazono *et al.*, "Development and performance test of a soft x-ray polarimeter and ellipsometer for complete polarization analysis," *Rev. Sci. Instrum.* **80**, 085109 (2009).

Non-Linear Relativistic Plasma Optics in a GeV Laser Wakefield Accelerator

Contact *m.streeter09@imperial.ac.uk*

M. J. V. Streeter, M. S. Bloom, A. Döpp, S. Kneip, S. P. D. Mangles, H. Nakamura and Z. Najmudin

Blackett Laboratory, Imperial College London, London SW7 2AZ, UK

R. A. Bendoyro, J. Jiang and N. C. Lopes

GoLP/Instituto de Plasmas e Fusão Nuclear, Instituto Superior Técnico, Lisboa, Portugal

O. Cheklov, C. Hooker, P. P. Rajeev and D. R. Symes

Central Laser Facility, STFC, Rutherford Appleton Laboratory, Didcot OX11 0QX, UK

J. Holloway

High Energy Physics Group, University College London, London WC1E 6BT, UK0

Introduction

Laser plasma wakefield accelerators have been successfully used to generate GeV quasi-monoenergetic electron beams over lengths of the order of 1 cm [1]. Acceleration to such energies requires the accelerating electric field, on the order of 100 GVm^{-1}, to be maintained over many times the vacuum Rayleigh range of a laser focus. This can be achieved with preformed guiding structures [2] or simply by using the self-focusing effects that occur for a relativistic intensity laser pulse propagating though a plasma [3]. In the latter case lateral refractive index gradients act as a focusing structure, which can balance the natural diffraction of the laser pulse. In addition, longitudinal variations in refractive index also cause the pulse to be modified spectrally and compressed temporally [4]. This can cause an increase in the intensity of the pulse which in turn changes the nature of the wake generated and can lead to self-injection of electrons. This non-linear interaction between the laser pulse and the plasma results in a complex acceleration process, and is critical to the quality and energy of the accelerated electron beams. Characterising the laser pulse as it exits the interaction can provide valuable information about the plasma conditions.

Experiment

An experiment was performed using the Astra Gemini Laser in the Central Laser Facility at the Rutherford Appleton Laboratory. Laser pulses were focused into a gas target to create a plasma wakefield and the transmitted pulses were characterised as shown in **figure 1**.

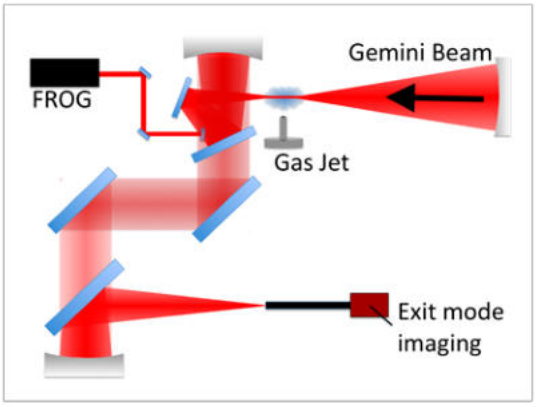

Figure 1: Experimental setup showing the optical diagnostics.

Each input pulse contained ≈ 12 J with a duration of ≈ 55 fs (FWHM) at a central wavelength of 800 nm. An f/20 off-axis parabolic mirror was used to create a 22 µm (FWHM) diameter focal spot containing ≈ 35 % of the energy. A 15 mm diameter super-sonic gas nozzle was used to create a conical region of helium gas which, when fully ionised, produced a plasma with density $n_e = 0 - 3.6 \times 10^{18}$ cm^{-3}. An f/10 spherical mirror allowed imaging of the exit plane of the gas jet. The imaging system had a resolution limit of 10 µm and a field of view of 902 × 675 µm. The integrated energy of the transmitted beam was measured by integrating the counts on the camera and cross-calibrated with an energy diode. Also a small region near the centre of the transmitted beam was directed into a Grenouille (Swamp Optics) SHG-FROG (second harmonic generation- frequency resolved optical gating). This device produced a spectrally dispersed auto-correlation of the pulse from which the complete temporal intensity and phase information of the pulse can be retrieved. A muti-step adaptive algorithm was used to retrieve the information of the pulse by minimising the error, defined as

$$E = \frac{1}{N}\sqrt{\sum_{p=1}^{p=N}\left(F_p - aG_p\right)},$$

where F is the measured FROG trace, G is the calculated FROG trace of a guess complex electric field, p is the grid index, N is the number of cells in the grid and a is a constant which minimises the error for a particular guess field. Only retrievals with errors of 0.02 or less were considered in the analysis for this report. A magnetic electron spectrometer was used to measure the spectrum of the accelerated electron beam. The data presented in this report is taken from a series of shots where the target density was varied in the range $n_e = 0 - 3.6 \times 10^{18}$ cm^{-3}.

Temporal characterisation of the laser pulse

The FWHM pulse duration of the retrieved pulses from the FROG are plotted in **figure 2**. As the density was increased the measured pulse duration decreased from an initial 55 fs to $10 - 20$ fs. For most of the shots it was not possible to determine the direction of time in the retrieved pulse field and the back propagation, to account for the glass in the beam, results in two possible answers for the temporal duration of the pulses. Above $n_e = 1.6 \times 10^{18}$ cm^{-3} high-energy electrons were observed on the spectrometer screens indicating that self-injection had occurred.

Pulse length shortening can occur due to pulse front etching [5] or self-phase modulation [6] and in general both of these occur. In the case of the latter, photon acceleration [7] results in spectral broadening and then the pulse is compressed by the group velocity dispersion in the wake. This results in an increase in the peak power of the pulse whereas pulse-front etching depletes energy from the pulse.

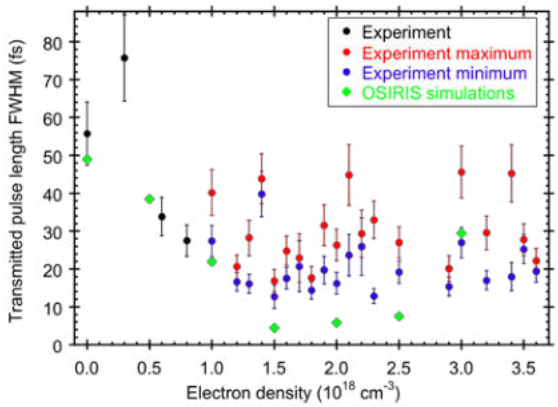

Figure 2: Transmitted pulse duration (FWHM) as a function of target electron density. Each point in the experimental data is averaged over shots within a bin width of 0.1 × 10^{18} cm^{-3}. Uncertainty in the direction of time gives two possible results for n_e > 1×10^{18} cm^{-3}. The error bars are the combination of the measurement errors and the standard error for each point.

Self-guiding of the laser pulse

Sample images from the exit mode imaging are shown in **figure 3** along with the corresponding images from the electron spectrometer.

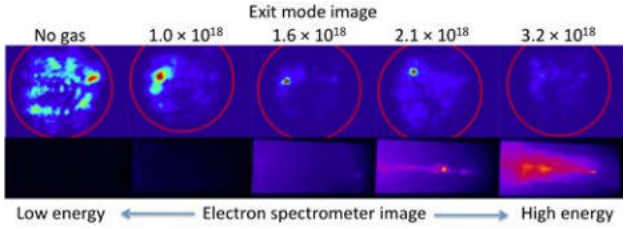

Figure 3: (Top) Spatial distribution of the transmitted laser pulse showing the vacuum beam size (red circle) and (Bottom) spectrometer screens showing the accelerated electrons (high energy to the right). The electron densities given above each pair of images are in cm^{-3}.

The exit mode imaging indicates that a significant fraction of the laser energy is trapped in the guided central channel for n_e > 1 × 10^{18} cm^{-3} with the channel diameter closely following the matched spot size given by $w_0 = 2\sqrt{a_0}c/\omega_p$. As the density increases further less energy remains in the guided spot as it is coupled into the wake. This coincides with a substantial increase in electron energy and flux indicating that self-injection has occurred. The energy outside of the guided channel has escaped the guiding plasma structure, either by diffraction of the leading edge or due to imperfect initial beam quality.

The transmitted laser energy is plotted in **figure 4** as well as the integrated signal observed on the electron spectrometer. This shows that the laser pulse is more strongly depleted as the density is increased. A sharp decrease in transmitted laser energy is observed in the density region where acceleration of significant charge electron bunches begins to occur, as more energy is coupled to the wake and into the accelerated electron beam. For n_e > 3 × 10^{18} cm^{-3} only the unguided fraction of the laser energy remains, corresponding to ≈10% of the input laser energy, although the pulse compression measurements indicate that some of the energy may been trapped for part of the propagation. This energy in the unguided region was seen to be weakly linearly dependant on density, increasing to ≈ 15% for n_e = 1 × 10^{18} cm^{-3}.

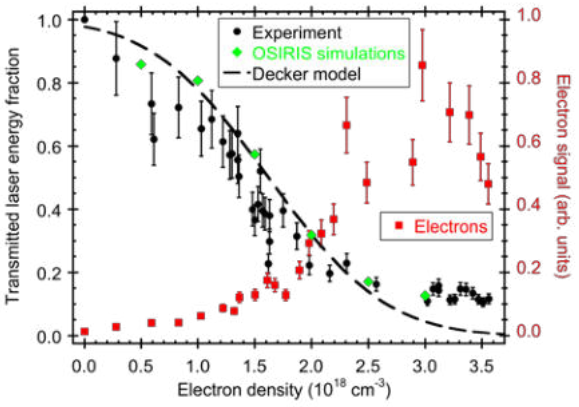

Figure 4: Transmitted pulse energy (black circles) and electron signal (red squares) as a function of gas density. Also shown are the transmitted energy calculated from OSIRIS simulations (green diamonds) and the Decker model prediction (dashed line) as described in the main text.

The Decker model [8] calculates the pump depletion rate as due to a density dependant pulse front etching velocity given by

$$v_{etch} = c\frac{\omega_p^2}{\omega_0^2} \quad .$$

The transmitted energy after 15 mm of propagation can be calculated by assuming a gaussian pulse with a FWHM of 50 fs enters the plasma and starts to be etched from the leading edge with $1/e^2$ of the peak. This is plotted alongside the experimental and simulation data in **figure 4** and shows good agreement with the observations.

The non-linear dephasing length [9] (the distance an electron can be accelerated for before leaving the region of the accelerating field), given by

$$L_d = \frac{4c\sqrt{a_0}}{3}\frac{\omega_0^2}{\omega_p^3} \quad ,$$

indicates the maximum acceleration in 15 mm of plasma will occur for n_e = 1.3 × 10^{18} cm^{-3}. As electron acceleration was seen to be optimal for greater densities this indicates that injection of electrons into the accelerating structure occurred after some propagation through the plasma. High-energy quasi-monoenergetic beams were observed for $n_e \approx 2.2 \times 10^{18}$ cm^{-3}, for which the dephasing length is 6.6 mm. This indicates that significant injection of charge occurs near the halfway point of the interaction, after the plasma effects have had time to modify the driving pulse. For higher densities, dephasing starts to reduce the energy and quality of the electron beams and the laser pulse is so depleted that it no longer drives a significant plasma wave. The electron beam can then begin to generate a plasma wakefield, further reducing the beam energy.

Simulations of propagation of the optical pulse

Simulations were performed using the OSIRIS [10] particle-in-cell code to model the evolution of the optical and plasma waves. The simulations were run in a moving box of 200 × 200 μm divided into 8000 by 800 cells. The pulse was modeled as a gaussian with FWHM duration of 50 fs, focused to a spot width FWHM of 25 μm and a peak a_0 of 3. The plasma target was 15 mm in length including initial and final density ramps over 500 μm. Five runs were performed with electron densities of n_e = 1, 1.5, 2, 3 and 4 cm^{-3} each with 4 particles per cell and stationary ions. The pulse duration of the transmitted pulse is determined by removing the rapidly oscillating component from the electromagnetic pulse after it exits the plasma and measuring the FWHM in the longitudinal direction. The transmitted energy is calculated by integrating the Poynting vector over the 2D plane. The results are plotted in **figures 2** and **4** alongside the experimental data.

Power amplification

Subtracting the unguided fraction from the transmitted energy gives the guided energy fraction for each density. The peak pulse power can then be calculated by setting the integral of the measured temporal shape to the guided energy for each density. The powers of the transmitted pulses, calculated in this way and then averaged into density bins of 0.1×10^{18} cm^{-3}, are plotted in **figure 5**. This shows that an increase in peak power was observed for shots in the density region of $n_e = 0.8 - 1.2 \times 10^{18}$ cm^{-3}.

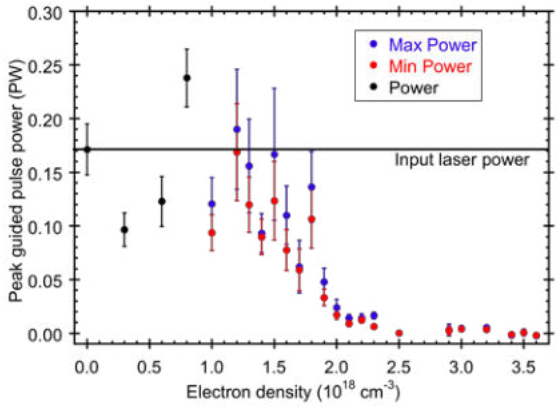

Figure 5: The peak pulse power plotted against gas electron density. The minimum and maximum powers are due to the uncertainty in the pulse measurements as discussed earlier.

Conclusions

Self-guiding of a relativistically intense laser beam through 15 mm of plasma has been observed leading to temporal compression from an initial 55 fs pulse down to 10 – 20 fs. This is accompanied by an increase in the laser power of ≈ 40%. The highest quality electron beams were observed in the density region where almost all of the guided laser energy is depleted. The dephasing length at these densities is much smaller than the gas jet diameter, indicating that the injection of electrons occurred after significant propagation through the plasma. The pulse shape modification and compression that occurs due to the longitudinal gradient in refractive index is vital to the acceleration process. For higher densities dephasing and pump depletion lead to a reduced electron beam energy and quality.

The observed dependence of laser depletion with plasma density is well approximated by a constant etching speed of a gaussian pulse, however the measurements of pulse compression and power amplification show that this is an over-simplistic model. PIC simulations have been shown to match the experimental results very well and therefore provide a useful tool for further study of the non-linear optics within laser driven wakefield accelerators. These suggest that pulse compression down to as short as 5 fs can occur while retaining 60% of the initial beam energy. Such pulses would be far more powerful than those of a similar pulse length generated in conventional laser systems.

Acknowledgements

The authors are very grateful for the excellent work of the CLF staff particularly those who ran the laser and provided technical support for the experiment.

References

1. W. P. Leemans et al., Nature Phys. **2**, 696 (2006); S. Kneip et al., Phys. Rev. Lett. **103**, 035002 (2009).
2. T. P. Rowlands-Rees et al., Phys. Rev. Lett **100**, 105005 (2008).
3. G. Z. Sun et al., Phys. Fluids **30**, 526 (1987); A. B. Borisov et al., Phys. Rev. Lett. **68**, 2309 (1992); A. G. Thomas, et al., Phys. Rev. Lett. **98**, 95004 (2007); J. E. Ralph, et al., Phys. Rev. Lett. **102**, 175003 (2009).
4. J. Faure, et al., Phys. Rev. Lett. **95**, 205003 (2005); J. Schreiber et al., Phys. Rev. Lett. **105**, 235003 (2010).
5. C. D. Decker et al., Physics of Plasmas **3**, 2047 (1996).
6. D. Gordon et al., Phys. Rev. Lett. **90**, 215001 (2003).
7. C. D. Murphy et al., Physics of Plasmas **13**, 33108 (2006).
8. C. D. Decker, et al., Physics of Plasmas **3**, 2047 (1996).
9. W. Lu et al., Phys. Rev. ST Accel. Beams **10**, 061301 (2007).
10. R. A. Fonseca, Lecture Notes in Computer Science (Springer, Heidelberg, (2002), **Vol.III-342**, p. 2329.